

Dark Matter Working Group: Draft of the 2HDM+a whitepaper

Authors missing!

Abstract. Let's play the music and not the background!

Contents

1	Evolution of theories for LHC DM searches	2
2	Description of the 2HDM+a model	5
3	Constraints on the 2HDM+a parameter space	6
4	Comparison to other DM models	11
5	E_T^{miss} signatures and their kinematic distributions	12
5.1	Resonant E_T^{miss} signatures	13
5.2	Non-resonant E_T^{miss} signatures	18
5.3	Parameter variations	20
6	Non-E_T^{miss} collider signatures	23
6.1	Di-top searches	24
6.2	Four-top searches	25
6.3	Other final states	27
7	Sensitivity studies	27
7.1	Mono-Higgs study	29
7.2	Mono- Z study	31
7.3	Sensitivity of other mono- X channels	33
A	Recasting procedure	33

1 Evolution of theories for LHC DM searches

The experimental results of two of the three DM search strategies, namely direct and indirect detection, are commonly interpreted in the DM effective field theory (DM-EFT) framework. The operators in these DM-EFTs are build from SM fermions and DM fields. Schematically, one has in the case of spin-0 interactions and Dirac fermion DM

$$\mathcal{L}_{\text{DM-EFT}} = \sum_{f=u,d,\ell} \left(\frac{C_1^f}{\Lambda^2} \bar{f} f \bar{\chi} \chi + \frac{C_2^f}{\Lambda^2} \bar{f} \gamma_5 f \bar{\chi} \gamma_5 \chi + \dots \right), \quad (1.1)$$

where the ellipsis represents additional operators not relevant for the further discussion, the sum over $f = u, d, \ell$ includes all SM quarks and leptons, the DM candidate is called χ and γ_5 denotes the fifth Dirac matrix. The above DM-EFT is fully described by the parameters

$$\{m_\chi, C_n^f/\Lambda^2\}. \quad (1.2)$$

Here m_χ is the mass of the DM candidate, Λ is the suppression scale of the higher-dimensional operators and the C_n^f are the so-called Wilson coefficients. Notice that Λ and C_n^f are not independent parameters but always appear in the specific combination given in (1.2).

The DM-EFT approach is justified for the small momentum transfer $q^2 \ll \Lambda^2$ in DM-nucleon scattering (set by the non-relativistic velocities of DM in the halo) and in DM annihilation (set by the mass of the annihilating DM candidate). See Figure 1 for an illustration of the relevant scales in each experiment. Early articles [1–6] on DM searches at colliders quantify the reach of the LHC in the parameter space in terms of (1.2) and similar operators. The momentum transfer at the LHC is however larger than the suppression scale, i.e. $q^2 \gg \Lambda^2$, for many theories of DM. In this case, the mediator of the interaction between the dark sector and the SM can be resonantly produced and predictions obtained using the DM-EFT framework often turn out to be inaccurate (see for instance [4, 7–13] and [14, 15] for exceptions).

The kinematics of on-shell propagators can be captured in DM simplified models, which aim to represent a large number of extensions of the SM, while keeping only the degrees of freedom relevant for LHC phenomenology [16, 17]. In the case of a pseudoscalar mediator a , the relevant DM-mediator and SM-mediator interactions read

$$\mathcal{L}_{\text{DM-SIMP}} = -ig_\chi a \bar{\chi} \gamma_5 \chi - ia \sum_j \left(g_u y_j^u \bar{u}_j \gamma_5 u_j + g_d y_j^d \bar{d}_j \gamma_5 d_j + g_\ell y_j^\ell \bar{\ell}_j \gamma_5 \ell_j \right), \quad (1.3)$$

with j representing a flavour index. Since the mediator a is a singlet it can also couple to itself and to $H^\dagger H$ where H denotes the SM Higgs doublet. The most general renormalisable scalar potential for a massive a is therefore

$$V_{\text{DM-SIMP}} = \frac{1}{2} m_a^2 a^2 + b_a a^3 + \lambda_a a^4 + b_H a H^\dagger H + \lambda_H a^2 H^\dagger H. \quad (1.4)$$

The parameters b_H and λ_H determine the couplings between the a and the H fields, thereby altering both the interactions and CP properties of the SM-like scalar h at 125 GeV as well

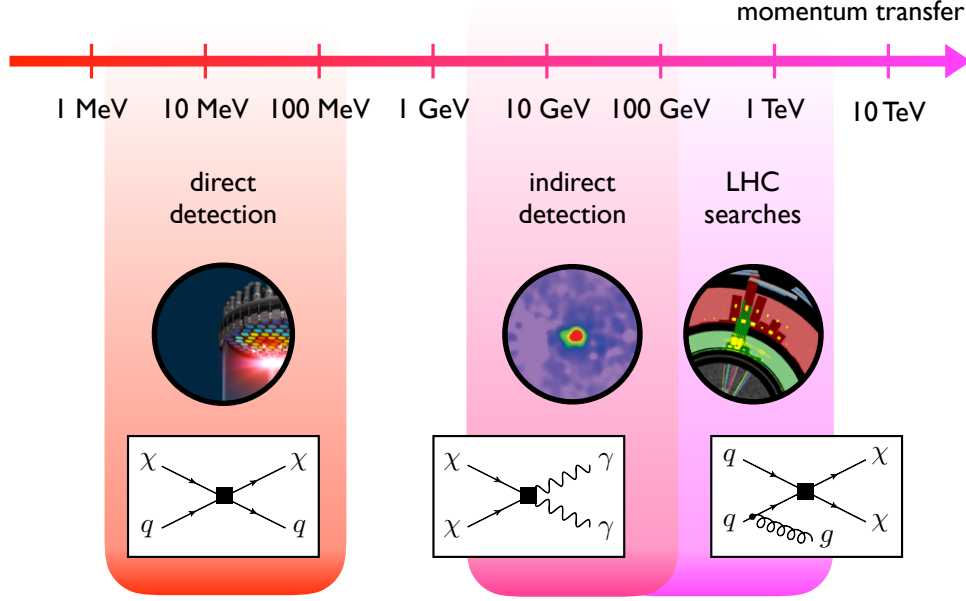


Figure 1: Range of momenta probed in direct-detection experiments, indirect-detection experiments and LHC searches. Prototypes of relevant Feynman diagrams are also shown.

as giving rise to possible new decay channels such as $h \rightarrow aa$ (see [18, 19] for details on the LHC phenomenology). Avoiding the resulting strong constraints for any choice of m_a , requires that $b_H \ll m_a$ and $\lambda_H \ll 1$. While the former requirement can be satisfied by imposing a Z_2 symmetry $a \rightarrow -a$, in the latter case one has to assume that λ_H is accidentally small if $m_a \lesssim 100 \text{ GeV}$ (cf. the related discussion on invisible decays of the Higgs boson in Section 3). Under such an assumption and noting that the self-coupling λ_a is largely irrelevant for collider phenomenology, the DM simplified model is fully described by the parameters

$$\{m_\chi, m_a, g_\chi, g_u, g_d, g_\ell\}. \quad (1.5)$$

In fact, in the limit of infinite mediator mass $m_a \rightarrow \infty$, the DM-SIMP Lagrangian (1.3) matches onto the DM-EFT Lagrangian (1.1). The corresponding tree-level matching conditions are $C_2^f/\Lambda^2 = g_\chi g_f y_f/m_a^2$ and $C_n^f = 0$ for all other Wilson coefficients.

Unfortunately, the operators in both $\mathcal{L}_{\text{DM-EFT}}$ and $\mathcal{L}_{\text{DM-SIMP}}$ violate gauge invariance, because the left- and right-handed SM fermions belong to different representations of the SM gauge group. In the case of the DM-EFT this suggests the Wilson coefficients C_n^f introduced in (1.1) actually scale as $C_n^f = c_n^f m_{f_i}/\Lambda$ [20], whereas for the DM simplified model restoring gauge invariance requires the embedding of the mediator a into an electroweak (EW) multiplet. The absence of gauge invariance leads to unitarity-violating amplitudes in DM simplified models (cf. [20–23]). In the case of the DM simplified model described by (1.3), one can show for instance that the amplitudes $\mathcal{A}(qb \rightarrow q'ta) \propto \sqrt{s}$ and $\mathcal{A}(gg \rightarrow Za) \propto \ln^2 s$ diverge in the limit of large center-of-mass energy s . The Feynman diagrams that lead to this behaviour are depicted on the left-hand side in Figure 2. Similar

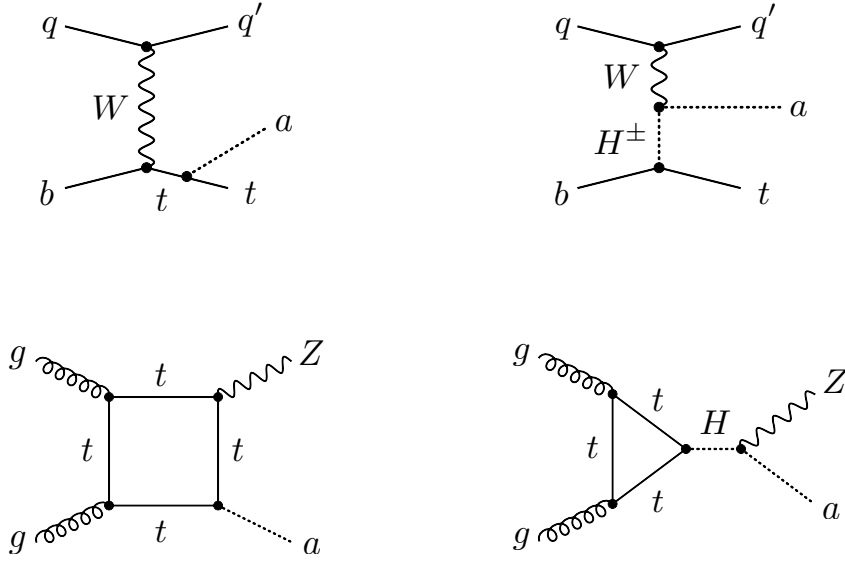


Figure 2: Diagrams contributing to the $qb \rightarrow q'ta$ (upper row) and $gg \rightarrow Za$ (lower row) scattering processes. Only the graphs on the left-hand side appear in the DM simplified model with a pseudoscalar, while in the 2HDM+a model in addition the diagrams on the right-hand side are present. See text for further details.

singularities appear in other single-top processes and in the mono-Higgs case. Since the divergences are not power-like, weakly-coupled realisations of (1.3) do not break down for the energies accessible at the LHC. The appearance of the \sqrt{s} and $\ln^2 s$ terms however signals the omission of diagrams that would be present in any gauge-invariant extension that gives rise to $\mathcal{L}_{\text{DM-EFT}}$ in the limit where all additional particles are heavy. For example, the $pp \rightarrow tja$ cross section is made finite by the exchange of a charged Higgs H^\pm , while in the case of $pp \rightarrow Za$ an additional scalar H unitarises the amplitude. The corresponding diagrams are displayed on the right in Figure 2. Notice that the cancellation of unitarity-violating terms among the diagrams of the latter figure is not at all accidental, but a direct consequence of the local gauge invariance of the underlying model.

The additional degrees of freedom necessary to unitarise the amplitudes cannot be arbitrarily heavy and hence may change the phenomenology of the DM simplified model. In fact, as can be seen from Figure 2, the presence of the H^\pm (H) allows to produce a mono-top (mono- Z) signal resonantly. Since resonant production is strongly enhanced compared to initial state radiation, the importance of the various mono- X signals in the extended DM model may then differ from the simplified model predictions [24–26]. In fact, we will see that in a specific extension of (1.3) called 2HDM+a model, the mono-Higgs, mono- Z and $tX + E_T^{\text{miss}}$ signals can be as or even more important than the $t\bar{t} + E_T^{\text{miss}}$ and mono-jet channel, which are the leading missing transverse energy (E_T^{miss}) signatures in the DM simplified pseudoscalar model [27–31]. We emphasise that the embedding of (1.3) is not unique, since both the mediator and the DM particle can belong to different EW

multiplets. In this whitepaper, we consider the simplest embedding with a single SM-singlet DM candidate, which captures the maximal number of interesting $E_{T,\text{miss}}$ signatures. We will briefly comment on other possible embeddings and related DM models in Section 4.

2 Description of the 2HDM+a model

The 2HDM+a model is a two Higgs doublet model (2HDM) that contains, besides the Higgs doublets H_1 and H_2 , an additional pseudoscalar singlet P . It is the simplest renormalisable extension of (1.3) with a SM-singlet DM candidate [24, 25, 32–34]. The gauge symmetry is made manifest by coupling the P to the dark Dirac fermion χ via

$$\mathcal{L}_\chi = -iy_\chi P \bar{\chi} \gamma_5 \chi, \quad (2.1)$$

while the Higgs doublets couple to the SM fermions through

$$\mathcal{L}_Y = - \sum_{i=1,2} \left(\bar{Q} Y_u^i \tilde{H}_i u_R + \bar{Q} Y_d^i H_i d_R + \bar{L} Y_\ell^i H_i \ell_R + \text{h.c.} \right). \quad (2.2)$$

Here y_χ is a dark-sector Yukawa coupling, Y_f^i are Yukawa matrices acting on the three fermion generations and we have suppressed flavour indices, Q and L are left-handed quark and lepton doublets, while u_R , d_R and ℓ_R are right-handed up-type quark, down-type quark and charged lepton singlets, respectively. Finally, $\tilde{H}_i = \epsilon H_i^*$ with ϵ denoting the two-dimensional antisymmetric tensor.

The particle that mediates the interactions between the dark sector and the SM is a superposition of the CP-odd components of H_1 , H_2 and P . We impose a Z_2 symmetry under which $H_1 \rightarrow H_1$ and $H_2 \rightarrow -H_2$, such that only one Higgs doublet appears in each operator in \mathcal{L}_Y . The different ways to construct these operators result in different Yukawa structures and in this whitepaper we will, for concreteness, consider only the so-called type-II 2HDM. This specific choice corresponds to setting $Y_u^1 = Y_d^2 = Y_\ell^2 = 0$ in (2.2). The Z_2 symmetry is the minimal condition necessary to guarantee the absence of flavour-changing neutral currents (FCNCs) at tree-level [35, 36] and such a symmetry is realised in many well-motivated complete ultraviolet (UV) theories in the form of supersymmetry, a $U(1)$ symmetry or a discrete symmetry acting on the Higgs doublets. We further choose all parameters in the scalar potential real, such that CP eigenstates are identified with the mass eigenstates, i.e. two scalars h and H , two pseudoscalars A and a and a charged scalar H^\pm . Under these conditions, the most general renormalisable scalar potential can be written as

$$V = V_H + V_{HP} + V_P, \quad (2.3)$$

with the potential for the two Higgs doublets

$$\begin{aligned} V_H = & \mu_1 H_1^\dagger H_1 + \mu_2 H_2^\dagger H_2 + \left(\mu_3 H_1^\dagger H_2 + \text{h.c.} \right) + \lambda_1 (H_1^\dagger H_1)^2 + \lambda_2 (H_2^\dagger H_2)^2 \\ & + \lambda_3 (H_1^\dagger H_1)(H_2^\dagger H_2) + \lambda_4 (H_1^\dagger H_2)(H_2^\dagger H_1) + \left[\lambda_5 (H_1^\dagger H_2)^2 + \text{h.c.} \right], \end{aligned} \quad (2.4)$$

potential terms which connect doublets and singlets

$$V_{HP} = P \left(i b_P H_1^\dagger H_2 + \text{h.c.} \right) + P^2 \left(\lambda_{P1} H_1^\dagger H_1 + \lambda_{P2} H_2^\dagger H_2 \right), \quad (2.5)$$

and the singlet potential

$$V_P = \frac{1}{2} m_P^2 P^2. \quad (2.6)$$

Notice that compared to [24, 32–34] which include only the trilinear portal coupling b_P , we follow [25] and also allow for quartic portal interactions proportional to λ_{P1} and λ_{P2} . A quartic self-coupling P^4 has instead not been included in (2.6), because such a term would not lead to any relevant effect in the E_T^{miss} observables studied in this whitepaper.

Upon rotation to the mass eigenbasis, we trade the five dimensionful and the eight dimensionless parameters in the potential for physical masses and mixing angles and four quartic couplings:

$$\left\{ \begin{array}{c} \mu_1, \mu_2, \mu_3, b_P, m_P, m_\chi \\ y_\chi, \lambda_1, \lambda_2, \lambda_3, \lambda_4, \lambda_5, \\ \lambda_{P1}, \lambda_{P2} \end{array} \right\} \longleftrightarrow \left\{ \begin{array}{c} v, M_h, M_A, M_H, M_{H^\pm}, M_a, m_\chi \\ \cos(\beta - \alpha), \tan \beta, \sin \theta, \\ y_\chi, \lambda_3, \lambda_{P1}, \lambda_{P2} \end{array} \right\}. \quad (2.7)$$

The parameters shown on the right-hand side of (2.7) will be used as input in the following. Out of these parameters, the EW vacuum expectation value (VEV) $v \simeq 246 \text{ GeV}$ and the mass of the SM-like CP-even mass eigenstate $M_h \simeq 125 \text{ GeV}$ are already fixed by observations. The experimental and theoretical constraints on the remaining parameter space will be examined in the next section.

3 Constraints on the 2HDM+a parameter space

In the following we examine the constraints on the input parameters (2.7) that arise from Higgs and flavour physics, LHC searches for additional Higgses, EW precision measurements and vacuum stability considerations. The discussed constraints will motivate certain parameter benchmarks. These will be summarised at the end of the section.

Constraints on $\cos(\beta - \alpha)$

The mixing angle α between the CP-even scalars h and H is constrained by Higgs coupling strength measurements and we display the regions in the $\cos(\beta - \alpha)$ – $\tan \beta$ plane that are allowed by the LHC Run-I combination [37] in the left panel of Figure 3. The shown 95% confidence level (CL) contour has been obtained in the type-II 2HDM. One observes that for arbitrary values of $\tan \beta$ only parameter choices with $\cos(\beta - \alpha) \simeq 0$ are experimentally allowed. To avoid the constraints from Higgs physics and to simplify the further analysis, we will concentrate in this whitepaper on the so-called alignment limit of the 2HDM where $\cos(\beta - \alpha) = 0$ [38], treating $\tan \beta$ as a free parameter.

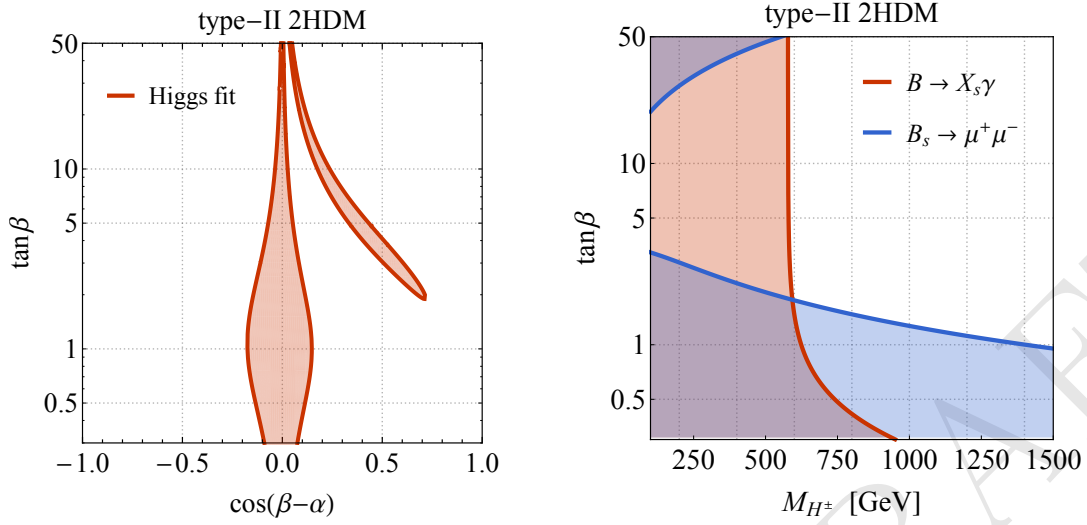


Figure 3: Left: Parameter space allowed by a global fit to the LHC Run-I Higgs coupling strength measurements. The lines show the contours which restrict the allowed parameter space at the 95% CL for a type-II 2HDM. Right: Parameter space in the $M_{H^\pm} - \tan\beta$ plane that is disfavoured by the flavour observables $B \rightarrow X_s \gamma$ (red) and $B_s \rightarrow \mu^+ \mu^-$ (blue). The uncoloured region in the upper right corner of the plot is allowed at 95% CL.

Constraints on $\tan\beta$

Indirect constraints on $\tan\beta$ as a function of M_{H^\pm} arise from $B \rightarrow X_s \gamma$ [39–41], B -meson mixing [42–45] as well as $B_s \rightarrow \mu^+ \mu^-$ [46–52], but also follow from $Z \rightarrow b\bar{b}$ [53–55]. For the case of the type-II 2HDM, the most stringent constraints on the $M_{H^\pm} - \tan\beta$ plane are depicted in the right panel of Figure 3. From the shown results it is evident that $B \rightarrow X_s \gamma$ provides a lower limit on the charged Higgs mass of $M_{H^\pm} > 580$ GeV that is practically independent of $\tan\beta$ for $\tan\beta \gtrsim 2$, while $B_s \rightarrow \mu^+ \mu^-$ is the leading constraint for very heavy charged Higgses, excluding for instance values of $\tan\beta < 1.3$ for $M_{H^\pm} = 1$ TeV. As discussed in Section 6, the constraints on $\tan\beta$ that follow from the existing LHC searches for heavy Higgses (see for instance [56–59]) are at the moment all weaker than the limits provided by flavour physics [25]. Since the indirect constraints arise from loop corrections they can in principle be weakened by the presence of additional particles that are too heavy to be produced at the LHC. We thus consider the bounds from flavour only as indicative, and will not directly impose them on the parameter space of the 2HDM+a in what follows.

Constraints on $\sin\theta$

EW precision measurements constrain the splittings between the masses M_H, M_A, M_{H^\pm} and M_a , since the exchange of spin-0 states modifies the propagators of the W - and Z -bosons at the one-loop level and beyond. For $M_H = M_{H^\pm}$ and $\cos(\beta - \alpha) = 0$, these corrections vanish due to a custodial symmetry in the tree-level potential V_H [60–64] introduced in (2.4) and the masses of the CP-odd mass eigenstates can be treated as free

parameters. This custodial symmetry is also present if $M_A = M_{H^\pm}$ and $\cos(\beta - \alpha) = 0$, but the presence of the pseudoscalar mixing term in (2.5) breaks this symmetry softly [25]. As a result, the pseudoscalar mixing angle θ and the mass splitting between M_H , M_A and M_a are constrained in such a case. An illustrative example of the resulting constraints is given in the left panel of Figure 4. To keep $\sin \theta$ and M_a as free parameters, we consider below only 2HDM+a model realisations in which the masses of the H , A and H^\pm are equal. Notice that the choice $M_H = M_A = M_{H^\pm}$ is also adopted in some 2HDM interpretations of the searches for heavy spin-0 resonances performed at the LHC (cf. [65–67] for example).

Constraints on M_a

Invisible decays of the Higgs boson allow to set a lower limit on the mass of the pseudoscalar a in 2HDM+a scenarios with light DM [25]. In the case of $m_\chi = 1$ GeV, it turns out for instance that mediator mass $M_a \lesssim 100$ GeV are excluded by imposing the 95% CL limit $\text{BR}(h \rightarrow \text{invisible}) \lesssim 25\%$ [68, 69]. This limit is largely independent of the choices of the other parameters since $\text{BR}(h \rightarrow \text{invisible}) \simeq \text{BR}(h \rightarrow aa^* \rightarrow 2\chi 2\bar{\chi}) \simeq 100\%$ for sufficiently light DM. To evade the limits from invisible Higgs decays, we consider in this whitepaper only a masses larger than 100 GeV when studying E_T^{miss} signatures at the LHC.

Constraints on λ_3

The requirement that the scalar potential (2.3) of the 2HDM+a is bounded from below (BFB), restricts the possible choices of the Higgs masses, mixing angles and quartic couplings. Assuming that $\lambda_{P1}, \lambda_{P2} > 0$, it is easy to see that the BFB conditions in the 2HDM+a are identical to those found in the pure 2HDM [38]. For our choice $M_H = M_A = M_{H^\pm}$ of heavy Higgs masses, one finds that the tree-level BFB conditions can be cast into two inequalities. The first inequality connects λ_3 with the cubic SM Higgs self-coupling $\lambda = M_h^2/(2v^2) \simeq 0.13$ and simply reads

$$\lambda_3 > 2\lambda. \quad (3.1)$$

The second BFB condition relates λ_3 with $\tan \beta$, $\sin \theta$, the common heavy Higgs mass M_H and M_a and turns out to be more complicated. In the limit $M_H \gg M_h, M_a$ it however takes a rather simple form that we quote here for illustration:

$$\lambda_3 > \frac{M_H^2 - M_a^2}{v^2} \sin^2 \theta - 2\lambda \cot^2(2\beta). \quad (3.2)$$

This formula in essence implies that large values of $M_H^2/v^2 \sin^2 \theta$ are only compatible with the requirements from BFB if the quartic coupling λ_3 is sufficiently large. Notice that the interplay between BFB and perturbativity of λ_3 , i.e. $\lambda_3 < 4\pi$, leads to a non-decoupling of H , A and H^\pm for $|M_H - M_a| \neq 0$ and $\sin \theta \neq 0$ [24] such that the spin-0 states are potentially within LHC reach. The right plot in Figure 4 which shows the constraints in the $M_a - M_H$ plane that derive from the exact version of (3.2) puts the latter statement on solid ground. From the figure one observes that for $\tan \beta = 1$, $\sin \theta = 0.35$ and $M_H = M_A = M_{H^\pm}$, values of $\lambda_3 \gtrsim 2$ are needed in order for $M_H \simeq 1$ TeV to be allowed by BFB. Notice that due to the $\sin^2 \theta$ dependence in (3.2), close to non-perturbative couplings $\lambda_3 \gtrsim 8$ would

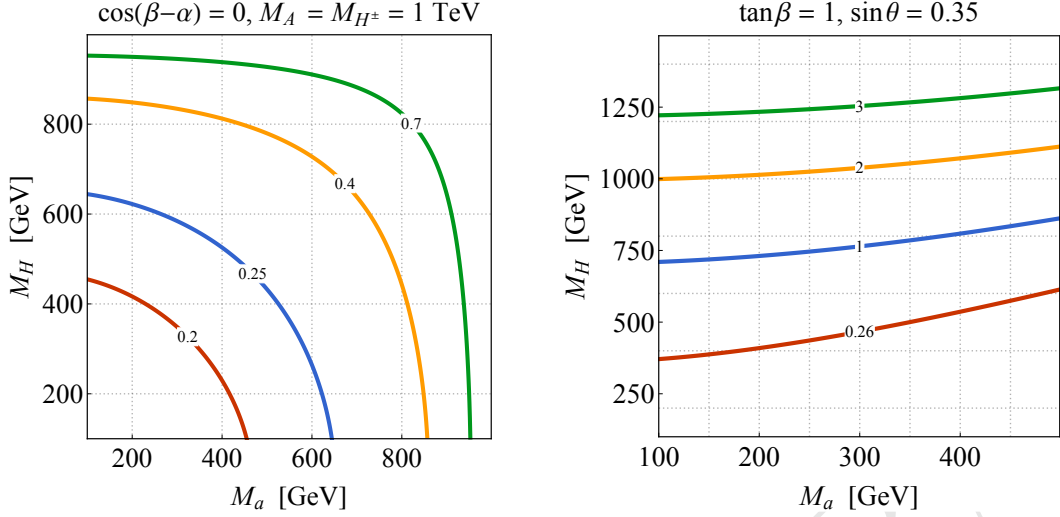


Figure 4: Left: Values of M_a and M_H allowed by EW precision constraints assuming $\cos(\beta - \alpha) = 0$, $M_A = M_{H^\pm} = 1$ TeV and four different values of $\sin \theta$, as indicated by the contour labels. The parameter space below and to the left of the contours is excluded. Right: Constraints in the $M_a - M_H$ plane following from the requirements of having a BFB 2HDM+a scalar potential. The shown results correspond to $\tan \beta = 1$, $\sin \theta = 0.35$ and degenerate heavy Higgs masses $M_H = M_A = M_{H^\pm}$. The region above each contour is excluded for the indicated value of λ_3 .

be required to make 1 TeV 2HDM Higgses viable for are larger pseudoscalar mixing angle of $\sin \theta = 0.7$. In order for heavy Higgs above 1 TeV to be acceptable while keeping λ_3 perturbative, we will choose $\sin \theta = 0.35$ and $\lambda_3 = 3$ as our benchmark in this whitepaper.

Constraints on λ_{P1} and λ_{P2}

The quartic couplings λ_3 , λ_{P1} and λ_{P2} affect all cubic Higgs interactions. In the case of the Haa and Aah couplings, one obtains under the assumption that $\cos(\beta - \alpha) = 0$ and $M_H = M_A = M_{H^\pm}$, the following expressions [25]

$$\begin{aligned} g_{Haa} &= \frac{1}{M_H v} \left[\cot(2\beta) (2M_h^2 - 2\lambda_3 v^2) \sin^2 \theta + \sin(2\beta) (\lambda_{P1} - \lambda_{P2}) v^2 \cos^2 \theta \right], \\ g_{Aha} &= \frac{1}{M_H v} \left[M_h^2 + M_H^2 - M_a^2 - 2\lambda_3 v^2 + 2(\lambda_{P1} \cos^2 \beta + \lambda_{P2} \sin^2 \beta) v^2 \right] \sin \theta \cos \theta. \end{aligned} \quad (3.3)$$

Because $\Gamma(H \rightarrow aa) \propto g_{Haa}^2$ and $\Gamma(A \rightarrow ha) \propto g_{Aha}^2$, the relations (3.3) imply that in order to keep the total widths Γ_H and Γ_A small, parameter choices of the form $\lambda_3 = \lambda_{P1} = \lambda_{P2}$ are well suited.

Benchmark parameter choices

The above discussion motivates the following choice of parameters

$$M_H = M_A = M_{H^\pm}, \quad m_\chi = 10 \text{ GeV},$$

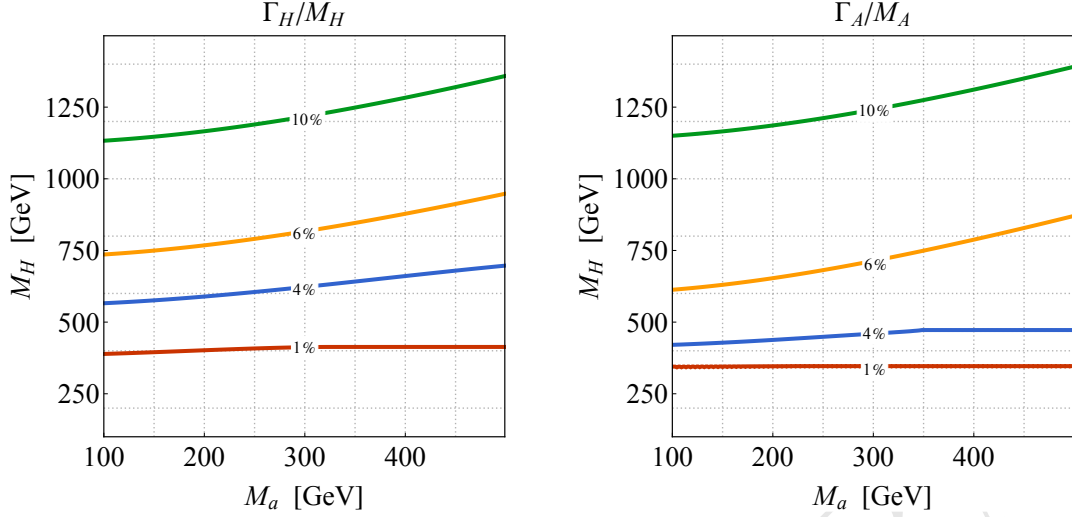


Figure 5: Predictions for Γ_H/M_H (left panel) and Γ_A/M_A (right panel). The shown results correspond to the type-II 2HDM+a benchmark parameter choices given in (3.4).

$$\begin{aligned} \cos(\beta - \alpha) &= 0, \quad \tan \beta = 1, \quad \sin \theta = 0.35, \\ y_\chi &= 1, \quad \lambda_3 = \lambda_{P1} = \lambda_{P2} = 3. \end{aligned} \quad (3.4)$$

In these type-II 2HDM+a benchmark scenarios the only free parameters are then M_H and M_a . We will study the sensitivity of the existing mono- X searches in the corresponding two-dimensional parameter plane in Section 7. Parameter scans in the $M_a - \tan \beta$ plane can also be found in this section. Apart from $\tan \beta$ which will be not fixed to 1 but allowed to vary freely, the latter scans will adopt the choices (3.4) with

$$M_H = M_A = M_{H^\pm} = 600 \text{ GeV}. \quad (3.5)$$

At this point it seems worthwhile to add that the mono- X signatures that are most sensitive to the mass splitting between the H and the A , the parameter $\sin \theta$ and the quartic couplings $\lambda_3, \lambda_{P1}, \lambda_{P2}$ turn out to be the mono-Higgs and mono- Z channels (see Section 5 for details). Four benchmark scenarios that illustrate these model dependences have been proposed and studied in [25]. We believe that the specific benchmarks chosen in (3.4) and (3.5) nicely exemplify the rich structure of E_T^{miss} signatures in the 2HDM+a model, and they should therefore serve well as a starting point for further more detailed experimental and theoretical investigations. Further parameter scans will be suggested in Section ??.

As a final validation (or first application) of the proposed benchmark scenario, we present in Figure 5 the predictions for the ratios Γ_H/M_H (left) and Γ_A/M_A (right). We see that the heavy neutral Higgs states H and A are relatively narrow even for values $M_H > 1 \text{ TeV}$ and $M_a = 100 \text{ GeV}$. The narrow width approximation (NWA) is thus applicable in the entire parameter space considered in our $M_a - M_H$ scans.

4 Comparison to other DM models

In this section we briefly discuss DM models that also feature a 2HDM sector. Our discussion will focus on the similarities and differences between these scenarios and the 2HDM+a model for what concerns the mono- X phenomenology.

2HDM with an extra scalar singlet

Instead of mixing an additional CP-odd singlet P with the pseudoscalar A , as done in (2.5), it is also possible to consider the mixing of a scalar singlet S with the CP-odd spin-0 states h, H . Detailed studies of the direct-detection and relic-density phenomenology of this so-called 2HDM+s model have been presented in [70, 71]. Like in the case of the 2HDM+a model, the presence of non-SM Higgs bosons in the 2HDM+s model can lead to novel E_T^{miss} signatures that are not captured by a simplified DM model with just a single scalar mediator. In the pure alignment limit, the most interesting collider signals are mono-Higgs, mono- Z and the $tX + E_T^{\text{miss}}$ channels, because these signatures can all arise resonantly. Away from alignment, the scalar mediator couples to the EW gauge bosons and as a result it may also be possible to have a sizeable amount of E_T^{miss} in association with a Z or W boson or in vector boson fusion (VBF). Notice that due to the CP properties of the a the latter E_T^{miss} signatures are not present in the 2HDM+a model.

2HDM with doublet-singlet DM

In both the 2HDM+a and the 2HDM+s model the DM particle is a EW singlet. The DM particle may however also be a mixture of a EW singlet and doublet(s) [72–75], as in the minimal supersymmetric SM where it has both bino and higgsino components. Generically, this is referred to as singlet-doublet DM. The phenomenology of 2HDM models with singlet-doublet DM has been discussed in [76, 77]. In these works only the $b + E_T^{\text{miss}}$ and $t\bar{t} + E_T^{\text{miss}}$ signatures have been considered and found to provide only weak constraints. The recent study [78] suggests that stronger constraints may arise in the 2HDM with doublet-singlet DM from $Z + E_T^{\text{miss}}$ and $tX + E_T^{\text{miss}}$ searches. This feature warrants further investigations.

2HDM with higher-dimensional couplings to DM

A gauge-invariant DM model where a pseudoscalar is embedded into a 2DHM that has renormalisable couplings to SM fields but an effective coupling to DM via the dimension-five operator $H_1^\dagger H_2 \bar{\chi} \gamma_5 \chi$ has been discussed in [78]. It has been shown that such an effective DM coupling can be obtained in different UV completions such as the 2HDM+a model or a 2HDM with doublet-singlet DM by integrating out heavy particles. Apart from the $tX + E_T^{\text{miss}}$ signatures, the whole suit of mono- X signals has been considered in [78]. It was found that a resonant mono- Z signal via $pp \rightarrow H \rightarrow AZ \rightarrow Z + \chi\bar{\chi}$ is a universal prediction in all DM pseudoscalar mediator models, while other signatures such as mono-Higgs are model dependent. Given that a sizeable $H^\pm \rightarrow AW$ rate is also a generic feature of DM pseudoscalar models if $M_{H^\pm} > M_A + M_W$, channels like $tW + E_T^{\text{miss}}$ [26] should also provide relevant constraints on the DM model introduced in [78].

Inert doublet model

In the scenarios discussed so far the DM particle has always been a fermion. The so-called inert doublet model (IDM) [79–81] is an intriguing DM model based on a 2HDM sector that can provide DM in the form of the spin-0 resonances H, A . A Z_2 symmetry renders the DM candidate stable and also implies that the bosonic states that originate from the second (dark) Higgs doublet can only be pair-produced. Since the dark scalars do not couple to the SM fermions, H, A, H^\pm production arises in the IDM dominantly from Drell-Yan processes. The IDM offers a rich spectrum of LHC E_T^{miss} signatures that ranges from mono-jet, mono- Z , mono- W , mono-Higgs to VBF + E_T^{miss} [82–92]. While the prospects to probe the IDM parameter space via the mono-jet channel seem to be limited [91], LHC searches for multiple leptons [82–85, 88, 89], multiple jets [87, 92] or a combination thereof [89] are expected to allow to test the IDM in limits that are not accessible by direct detection of DM or measurements of the invisible decay width of the SM Higgs. Furthermore, in scenarios in which the mass of DM is almost degenerate with M_{H^\pm} , searches for disappearing charged tracks provide a rather unique handle on the IDM high-mass regime [91]. Notice that while the IDM can lead to the same E_T^{miss} signals than the 2HDM+a model, the resulting kinematic distributions will in general not be the same, due to the different production mechanisms and decay topologies in the two models. Selection cuts that are optimised for a 2HDM+a interpretation of a given mono- X search will thus often not be ideal in the IDM context. Dedicated ATLAS and CMS analyses of the mono- X signatures in the IDM do unfortunately not exist at the moment. Such studies would however be highly desirable.

2HDM with an extra scalar mediator and scalar DM

The DM scenario proposed in [93] contains like the 2HDM+s model an extra scalar singlet, which however does not couple to a fermionic DM current $\bar{\chi}\chi$ but to the scalar operator χ^2 . The latter work focuses on the parameter space of the model where the mediator s is dominantly produced via either $pp \rightarrow H + j \rightarrow 2s + j \rightarrow j + 4\chi$ or $pp \rightarrow H \rightarrow sh \rightarrow h + 2\chi$. The resulting mono-jet and mono-Higgs cross sections however turn out to be safely below the existing experimental limits. In case the mass hierarchy $M_A > M_H + M_Z$ is realised, the channel $pp \rightarrow A \rightarrow HZ$ is also interesting, since it either leads to a mono- Z or a $Zh + E_T^{\text{miss}}$ signature, depending on whether $H \rightarrow 2s \rightarrow 4\chi$ or $H \rightarrow hs \rightarrow h\chi^2$ is the leading decay. We add that an effective version of the model brought forward in [93] has already been constrained by ATLAS [94] using the mono-Higgs channel.

5 E_T^{miss} signatures and their kinematic distributions

The mono- X phenomenology in the 2HDM+a model is determined by the values of the parameters introduced in (2.7). These model parameters can affect the total signal cross sections of the E_T^{miss} signatures, their kinematic distributions, or both. In this section we will discuss the basic features of the most important mono- X channels and identify the experimental observables that can be exploited to search for them. Our discussion will mainly focus on the benchmark (3.4) but we will also present results for other parameter choices to illustrate how a given parameter affects a certain E_T^{miss} signature. All results

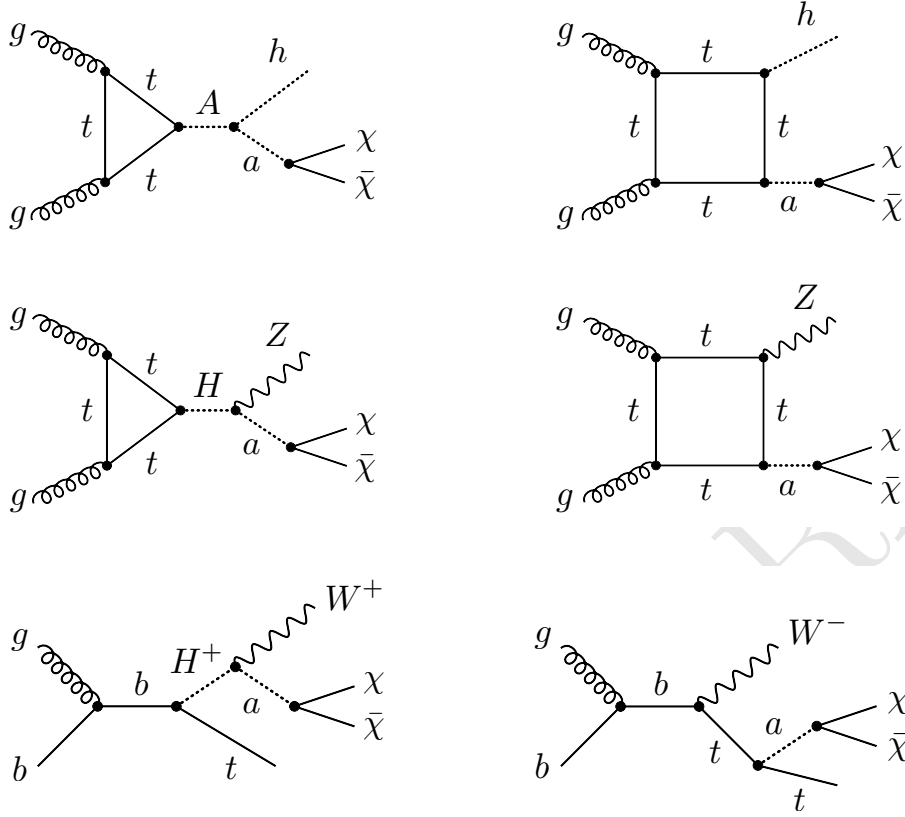


Figure 6: Example diagrams that give rise to a $h + E_T^{\text{miss}}$ (upper row), $Z + E_T^{\text{miss}}$ (middle row) and $tW + E_T^{\text{miss}}$ (lower row) signal in the 2HDM+a model. For further details consult the main text.

in this section are obtained at the particle level and employ no or only minimal selection requirements.

5.1 Resonant E_T^{miss} signatures

Broadly speaking, in the 2HDM+a model there are two different kinds of E_T^{miss} signatures. Signals of the first type can be resonantly produced [Caterina: "signals can be resonantly produced" may not be the clearest sentence for an experimental newcomer, but I'm not sure of how to clarify this.] and channels such as $h + E_T^{\text{miss}}$, $Z + E_T^{\text{miss}}$ and $tW + E_T^{\text{miss}}$ belong to this class. Relevant examples of Feynman graphs are shown in Figure 6. In the case of the mono-Higgs signature, it is evident from the figure that for $M_A > M_h + M_a$ the triangle graph depicted on the left in the upper row allows for resonant mono-Higgs production. Similar resonance enhancements arise from the diagram on the left-hand side for the mono-Z (middle row) and $tW + E_T^{\text{miss}}$ (lower row) channel if $M_H > M_Z + M_a$ and $M_H^\pm > M_W + M_a$, respectively. Notice that resonant $h + E_T^{\text{miss}}$, $Z + E_T^{\text{miss}}$ and $tW + E_T^{\text{miss}}$ production is not possible in the spin-0 DM models proposed by the DM forum (DMF) [17] because in these models the mediators couple only to fermions at tree level. As a result

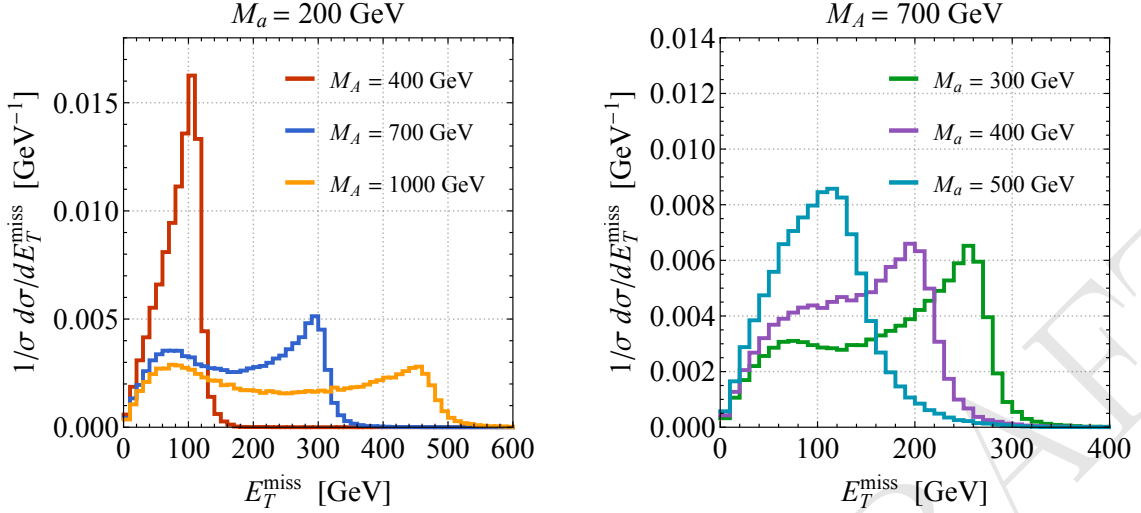


Figure 7: Normalised E_T^{miss} distributions of mono-Higgs production in the 2HDM+a model for different values of M_A and M_a as indicated in the legends. The shown results correspond to the benchmark parameter choices introduced in (3.4). [Caterina: are those at parton level?]

only diagrams of the type shown on the right-hand side of the latter figure are present in these models.

Mono-Higgs signature

Processes that are resonantly enhanced in the 2HDM+a model have in common that they involve the on-shell decay of a heavy Higgs H, A, H^\pm to a SM particle and the mediator a , which itself subsequently decays to a pair of DM particles. The kinematics of the process $A \rightarrow BC$ is governed by the two-body phase space for three massive particles

$$\lambda(m_A, m_B, m_C) = (m_A^2 - m_B^2 - m_C^2)^2 - 4m_B^2 m_C^2, \quad (5.1)$$

and this quantity determines the characteristic shape of resonant E_T^{miss} signals in the context of the 2HDM+a model. For instance, in the case of the mono-Higgs signal the E_T^{miss} spectrum will have a Jacobian peak with an endpoint at [25, 33]

$$E_{T,\text{max}}^{\text{miss}} \simeq \frac{\lambda^{1/2}(M_A, M_h, M_a)}{2M_A^2}, \quad (5.2)$$

for all mass configurations that satisfy $M_A > M_h + M_a$.

In Figure 7 we show the predictions for the normalised E_T^{miss} distribution of $h + E_T^{\text{miss}}$ production in the 2HDM+a model for different Higgs masses M_A and M_a . Besides the indicated values of M_A and M_a the parameters used are those given in (3.4). As can be seen from the figure, increasing M_A (M_a) shifts the endpoint of the Jacobian peak to higher (lower) E_T^{miss} values as expected from (5.2). A second feature that is also visible is the plot is that for large mass splittings $M_A - M_a$, the E_T^{miss} spectra develop a pronounced

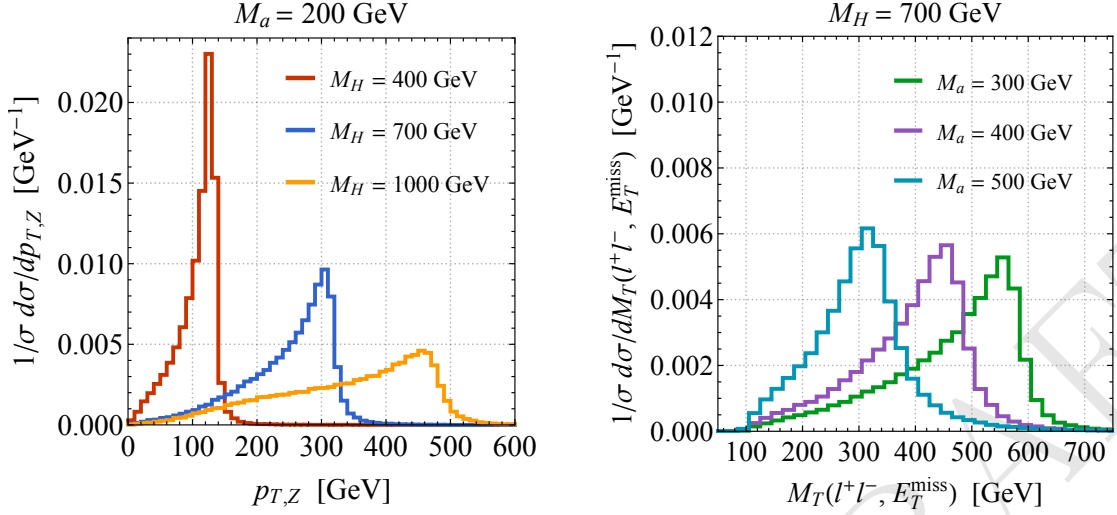


Figure 8: Normalised $p_{T,Z}$ (left panel) and $M_T(\ell^+\ell^-, E_T^{\text{miss}})$ (right panel) distributions for $Z + E_T^{\text{miss}}$ production followed by $Z \rightarrow \ell^+\ell^-$. The shown predictions have been obtained for the 2HDM+a benchmark parameter choices given in (3.4) and employ different values of M_H and M_a as indicated in the legends.

low- E_T^{miss} tail. The events in these tails arise dominantly from the box diagram shown on the right in the upper row of Figure 6. One can also see that these non-resonant contributions interfere with the resonant contributions that stem from triangle graphs. Due to the interplay of resonant and non-resonant contributions the exact shape of the E_T^{miss} distribution is away from the endpoint (5.2) a non-trivial function of the 2HDM+a parameters (2.7).

At the LHC a mono-Higgs signal has so far been searched for in the $h \rightarrow \gamma\gamma$ and the $h \rightarrow b\bar{b}$ channel (see [94–96] for the latest ATLAS and CMS results). While both searches use E_T^{miss} as the main selection variable to discriminate signal from background, the E_T^{miss} values for which the $\gamma\gamma + E_T^{\text{miss}}$ search is most sensitive are smaller than those that give the highest sensitivity in the case of $b\bar{b} + E_T^{\text{miss}}$. This feature makes the two modes complementary in the sense that a models with small splittings $M_A - M_a$ are best probed in the former channel, while realisations with a larger mass hierarchy can be well tested via the latter final state. The decay channel $h \rightarrow WW$ also offers interesting prospects to search for a mono-Higgs signal in the 2HDM+a model [97] but as yet has not been studied by the LHC collaborations. Auxiliary figures showing mono-Higgs distributions in the 2HDM+a model can be found in Appendix ??.

Mono- Z signature

Like for the mono-Higgs signal also in the mono- Z case shape analyses of the E_T^{miss} variable offer a powerful way to enhance the signal-to-background ratio. The endpoint of the E_T^{miss} spectrum for the $Z + E_T^{\text{miss}}$ signature can be simply obtained from (5.2) by the replacements $M_A \rightarrow M_H$ and $M_h \rightarrow M_Z$. Plots that show the corresponding E_T^{miss} distributions can be found in Appendix ??.

enter $H \rightarrow Za$ are fixed by H being preferentially on-shell, also the spectrum of the Z -boson transverse momentum ($p_{T,Z}$) in mono- Z production will have a characteristic shape if $M_H > M_Z + M_a$. In fact, the $p_{T,Z}$ distribution is like the E_T^{miss} spectrum predicted to be Jacobian with a cut-off at [25, 33]

$$p_{T,Z}^{\text{max}} \simeq \frac{\lambda^{1/2}(M_H, M_Z, M_a)}{2M_H^2}, \quad (5.3)$$

that is smeared by the total decay width Γ_H of the heavy Higgs H . Notice that ignoring parton-shower and detector effects the shapes of the $p_{T,Z}$ and E_T^{miss} spectra are identical. Whether a shape fit to E_T^{miss} or $p_{T,Z}$ provides a better experimental reach thus depends to first approximation only on which of the two variables can be better measured.

Another useful observable to study the properties of processes involving visible and invisible decay production is the transverse mass

$$M_T(A, B) = \sqrt{m_A^2 + m_B^2 + 2(E_{T,A}E_{T,B} - \vec{p}_{T,A} \cdot \vec{p}_{T,B})}, \quad (5.4)$$

where $E_{T,A}$ ($E_{T,B}$) denotes the transverse energy of the final-state configuration A (B) and $\vec{p}_{T,A}$ ($\vec{p}_{T,B}$) is the corresponding transverse momentum three-vector. In the case of the mono- Z search that looks for the leptonic decay of the Z boson, the transverse mass can be constructed from the $\ell^+\ell^-$ system and the amount of E_T^{miss} .

Figure 8 displays $p_{T,Z}$ and $M_T(\ell^+\ell^-, E_T^{\text{miss}})$ distributions for different choices of the masses M_H and M_a . The parameters not explicitly specified in the plots have been fixed to the values reported in (3.4). One observes that the differential distributions in $p_{T,Z}$ and $M_T(\ell^+\ell^-, E_T^{\text{miss}})$ have Jacobian peaks, a feature that reflects the resonant production of a H with the subsequent decay $H \rightarrow Za \rightarrow \ell^+\ell^-\chi\bar{\chi}$. Increasing M_H (M_a) again shifts the endpoints of the distributions to higher (lower) values of $p_{T,Z}$ and $M_T(\ell^+\ell^-, E_T^{\text{miss}})$. Like in the mono-Higgs case, for large mass differences $M_H - M_a$, box diagrams lead to a non-negligible mono- Z rate at low values of $p_{T,Z}$ and $M_T(\ell^+\ell^-, E_T^{\text{miss}})$. Compared to the $h+E_T^{\text{miss}}$ signature the interference effects between resonant and non-resonant contributions are however less pronounced in the $Z + E_T^{\text{miss}}$ case. Plots showing additional mono- Z distributions are provided in Appendix ??.

The existing LHC searches for a mono- Z signal (cf. [98, 99] for the most recent results) have focused either on invisible decays of the SM-like Higgs boson or on topologies where the Z boson is produced in the form of initial-state radiation (ISR). Since ISR of a Z boson is compared to the radiation of a gluon suppressed by both the coupling of the Z and its mass, the mono- Z signal is generically not a discovery channel in models that lead to ISR-like mono- X signatures. In contrast, in the 2HDM+a model the $Z + E_T^{\text{miss}}$ sensitivity turns out to be typically better than the one of the mono-jet channel.

The above discussion has focused on the leptonic decay of the Z boson but searching for a mono- Z signal in the hadronic channel is also possible. In fact, the hadronic and leptonic signatures are complementary, since hadronic decays of the Z boson are more frequent than leptonic decays, but suffer from larger backgrounds. An improved background suppression is possible if “boosted” event topologies are studied, making the hadronic mono- Z

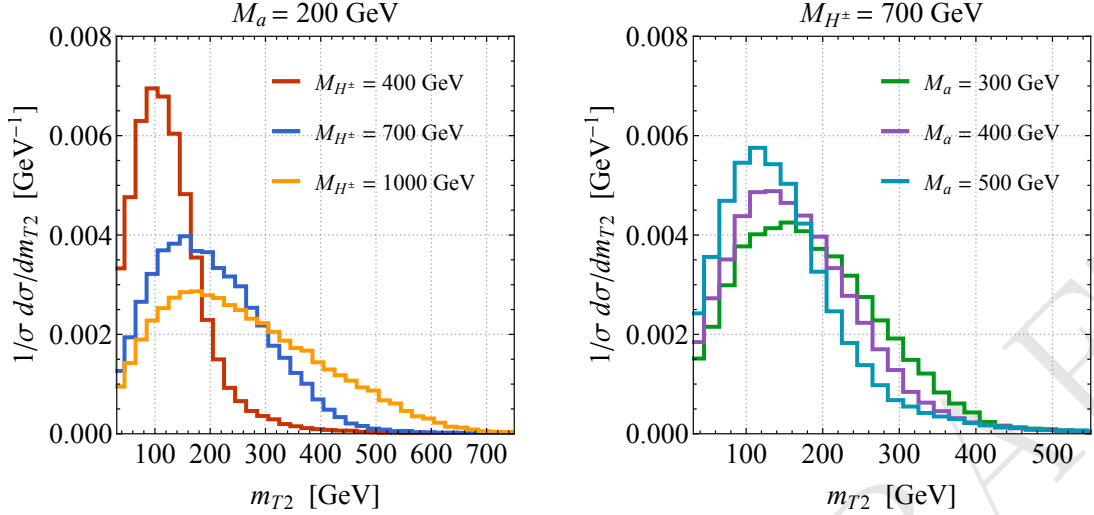


Figure 9: Normalised m_{T2} distributions for $tW + E_T^{\text{miss}}$ production in the double-lepton channel. The shown results correspond to the 2HDM+a benchmark (3.4) and employ different values of M_{H^\pm} and M_a as indicated in the legends.

signature an interesting channel if the 2HDM+a model includes high-mass Higgs states. Further details on $q\bar{q} + E_T^{\text{miss}}$ search strategies can be found in Appendix ?? [Caterina: add CONF note from ATLAS <https://cds.cern.ch/record/2311941/> and monojet from CMS]

Single-top signatures

Single-top production in association with E_T^{miss} has also been shown to be a promising mono- X channel in the case of spin-0 models [26, 100, 101]. One can study single-top production in the s -channel, t -channel or in association with a W boson. In the following, we will focus on the $tW + E_T^{\text{miss}}$ channel, which in the context of the 2HDM+a model has been identified as the most interesting mode [26]. Example diagrams leading to a $tW + E_T^{\text{miss}}$ signature are shown in the lower row of Figure 6. The $tW + E_T^{\text{miss}}$ signal can be searched for in the single-lepton and double-lepton final state. Analysis strategies for both channels have been developed in [26]. In the former case $M_T(\ell, E_T^{\text{miss}})$ and the asymmetric transverse mass am_{T2} [102, 103] can be used to discriminate between signal and background, while in the latter case the transverse mass m_{T2} [104, 105] plays a crucial role in the background suppression. [Caterina: worth defining MT2?]

Examples of normalised m_{T2} distributions obtained in the 2HDM+a model are shown in Figure 9. The coloured histograms correspond to different masses M_{H^\pm} and M_a . The parameters not indicated in the legends have been set to the values given in (3.4). One sees from the plots that the shape of the m_{T2} spectrum is sensitive to the values that are chosen for M_{H^\pm} and M_a . In particular, the maximum of the m_{T2} distribution is shifted to higher values for larger (smaller) values of M_{H^\pm} (M_a). Notice that for heavy charged Higgses the m_{T2} spectrum develops a pronounced high- m_{T2} tail. This feature can be traced back to the resonant contribution $bg \rightarrow tH^+ \rightarrow tW^+a \rightarrow tW^+\chi\bar{\chi}$ (see lower left graph in Figure 6). At present, dedicated ATLAS and CMS analyses of the $tW + E_T^{\text{miss}}$ or other

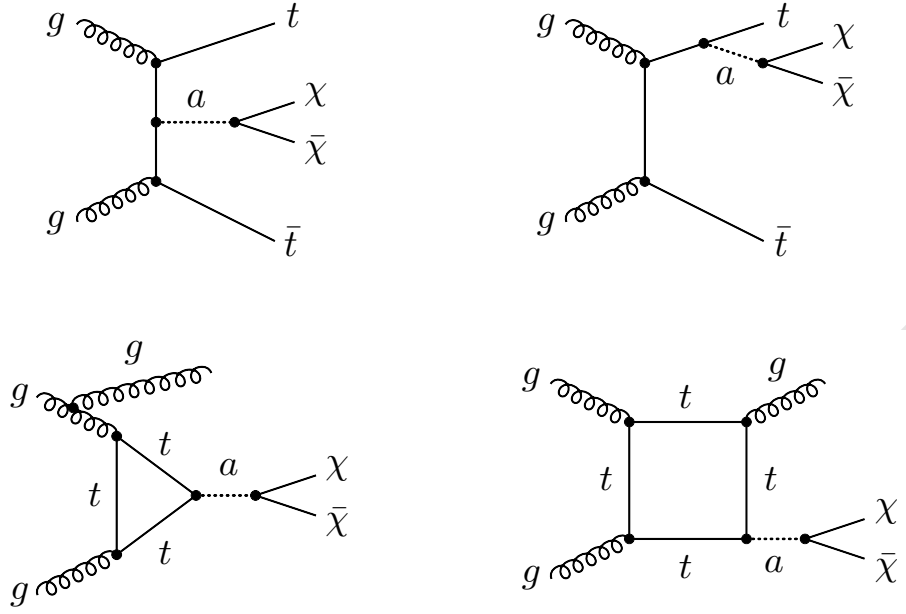


Figure 10: Prototype diagrams that lead to a $t\bar{t} + E_T^{\text{miss}}$ (upper row) and $j + E_T^{\text{miss}}$ (lower row) signal in the 2HDM+a model. Graphs involving a heavier pseudoscalar A also contribute to the signals but are not shown explicitly.

single-top-like signatures with E_T^{miss} do not exist. Performing such studies would however be worthwhile since enhanced single-top signatures are expected to appear in many DM model that features an extended Higgs sector.

5.2 Non-resonant E_T^{miss} signatures

Besides the resonant E_T^{miss} signatures discussed in the last subsection the 2HDM+a model also gives rise to non-resonant mono- X signatures. The most important channels in this class are $t\bar{t} + E_T^{\text{miss}}$ and $j + E_T^{\text{miss}}$ production, but also the $b\bar{b} + E_T^{\text{miss}}$ mode is interesting because its rate is $\tan\beta$ enhanced if a Yukawa sector of type-II is realised. Representative Feynman graphs leading to the first two signatures are depicted in Figure 10. Notice that for $M_A \gg M_a > 2m_\chi$ the dominant contribution to the $t\bar{t} + E_T^{\text{miss}}$ and mono-jet signals arise from graphs involving the mediator a . In this limit the normalised kinematic distributions of the $t\bar{t} + E_T^{\text{miss}}$ and $j + E_T^{\text{miss}}$ signals in the 2HDM+a model therefore resemble the shapes of the spectra obtained in the DMF pseudoscalar model. Since the contributions associated to a and A exchange interfere with each other, shape differences can however occur if the pseudoscalars are not widely separated in mass [25].

Heavy-quark signatures

Two of the main channels that have been used up to now to search for spin-0 states with large invisible decay widths at the LHC are $t\bar{t} + E_T^{\text{miss}}$ and $b\bar{b} + E_T^{\text{miss}}$. The latest ATLAS and CMS analyses of this type can be found in [106, 107]. These searches have been interpreted

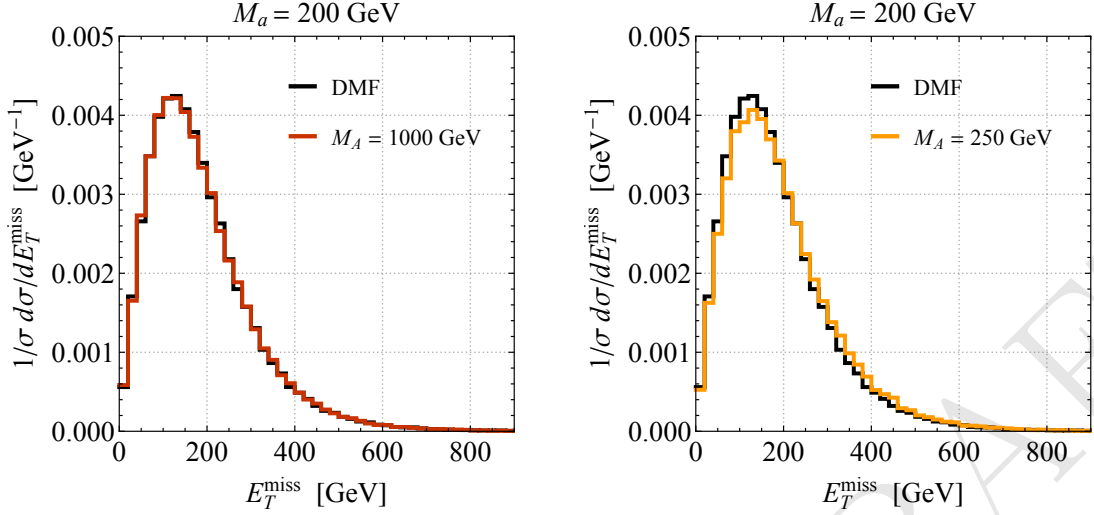


Figure 11: Normalised E_T^{miss} distributions for $t\bar{t} + E_T^{\text{miss}}$ production. The black curves correspond to the prediction of the DMF pseudoscalar model, while the coloured predictions illustrate the results in the 2HDM+a benchmark model (3.4) for two different choices of M_A and M_a .

in the context of the DMF spin-0 models, and for $M_A \gg M_a$ the obtained cross-section limits can be used to derive exclusion bounds in the 2HDM+a model by using [25]

$$\frac{\sigma(pp \rightarrow t\bar{t} + E_T^{\text{miss}})_{\text{2HDM+a}}}{\sigma(pp \rightarrow t\bar{t} + E_T^{\text{miss}})_{\text{DMF}}} \simeq \left(\frac{y_\chi \sin \theta}{g_\chi g_q \tan \beta} \right)^2. \quad (5.5)$$

Here g_χ (g_q) denotes the DM-mediator (universal quark-mediator) coupling in the DMF pseudoscalar model, and an analog formula holds in the case of the $b\bar{b} + E_T^{\text{miss}}$ signature with $\tan \beta$ replaced by $\cot \beta$ in the type-II 2HDM+a model.

In Figure 11 we compare two normalised E_T^{miss} spectra obtained in the 2HDM+a model (coloured histograms) to the prediction of the DMF pseudoscalar model (black histograms). The left panel illustrates the case $M_A \gg M_a$, and one observes that the shape of the 2HDM+a distribution resembles the one of the DMF model within statistical uncertainties. As shown in the plot on the right-hand side, shape distortions instead arise if the particle masses M_A and M_a are not widely separated. Similar findings apply to other variables such as m_{T2} which plays a crucial role in suppressing the $t\bar{t}$ background in two-lepton analyses of the $t\bar{t} + E_T^{\text{miss}}$ signature [106, 108]. It follows that in order to accurately reproduce the kinematic distributions of the signal in the entire 2HDM+a parameter space, one should not rely on (5.5) but should use a more sophisticated method. A general approach that allows to faithfully translate existing limits on DMF spin-0 models into the 2HDM+a parameter space is described in Appendix A. There it is also shown that this rescaling procedure reproduces the results of a direct MC simulation.

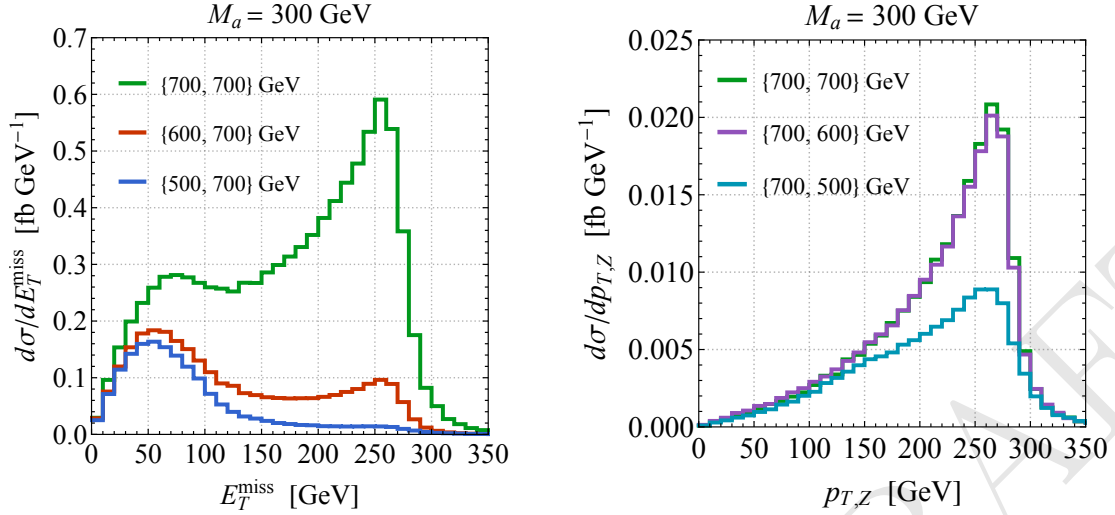


Figure 12: $E_T^{\text{miss}}(p_{T,Z})$ distributions for mono-Higgs (mono- Z) production at 13 TeV in the 2HDM+a model. The shown predictions correspond to different sets $M_{H,A}$ of masses and employ $M_{H^\pm} = \min(M_H, M_A)$, $M_a = 300$ GeV as well as the parameters (3.4).

Mono-jet signature

At the LHC the most studied mono- X signal is the $j + E_T^{\text{miss}}$ channel (the newest analyses have been presented in [109, 110]) because this mode typically provides the strongest E_T^{miss} constraints on models with ISR-type signatures. Since only loop diagrams where a mediator couples to a quark (see the graphs in lower row in Figure 10) contribute to the mono-jet signature in both the 2HDM+a and the DMF spin-0 models, the normalised kinematic distributions of the $j + E_T^{\text{miss}}$ signal is very similar in these models. In the case that the 2HDM pseudoscalar A is decoupled one can use a relation similar to the one shown in (5.5) to translate the existing mono-jet results on the DMF pseudoscalar model into the 2HDM+a parameter space, while in general one can apply the recasting procedure detailed in Appendix A.

5.3 Parameter variations

The kinematic distributions shown in Sections 5.1 and 5.2 all employ the parameters (3.4) and consider only variations of the common heavy Higgs mass $M_H = M_A = M_{H^\pm}$ and the mediator mass M_a . In this subsection we study the impact that modifications of the parameters away from the proposed 2HDM+a benchmark scenarios have. The discussion will thereby focus on the mono-Higgs and mono- Z signatures since the rates and kinematic distributions of these two channels turn out to be most sensitive to parameter changes.

Variations of M_H and M_A

In Figure 12 we display E_T^{miss} distributions in $h + E_T^{\text{miss}}$ production (left panel) and $p_{T,Z}$ distributions in $Z + E_T^{\text{miss}}$ production (right panel) for different M_H and M_A values. As indicated, the coloured histograms correspond to different choices of $M_{H,A}$ and

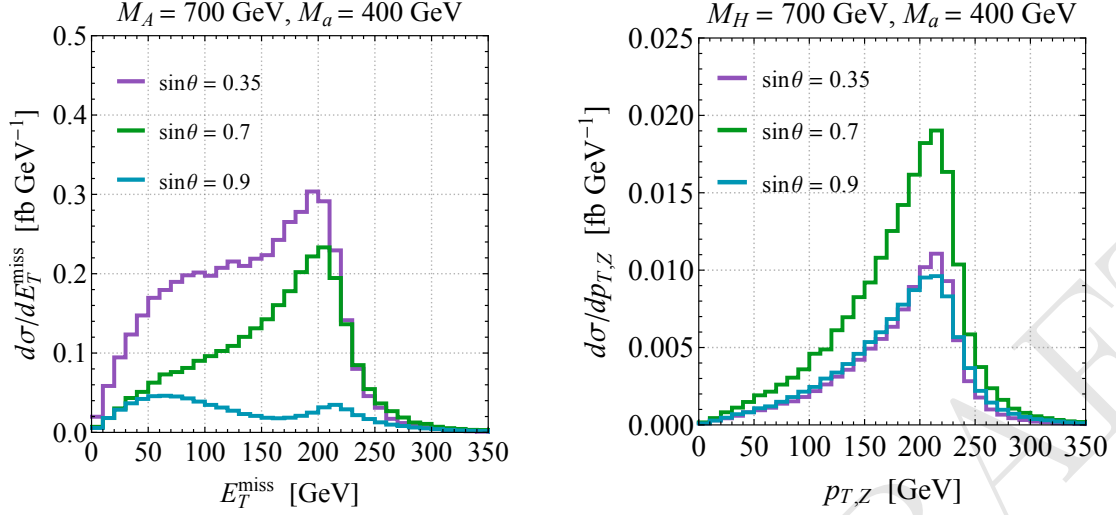


Figure 13: E_T^{miss} ($p_{T,Z}$) distributions for mono-Higgs (mono- Z) production at 13 TeV in the 2HDM+a model. The displayed results correspond to different choices of $\sin\theta$. The remaining parameters are fixed to (3.4) using $M_H = M_A = M_{H^\pm} = 700$ GeV and $M_a = 400$ GeV.

$M_{H^\pm} = \min(M_H, M_A)$, but all employ $M_a = 300$ GeV. From the figure it is evident that the inclusive mono-Higgs (mono- Z) cross section is reduced compared to the benchmark prediction if M_H (M_A) is taken to be smaller than M_A (M_H). We furthermore observe that a change of M_H strongly affects the shape of the E_T^{miss} distribution, while the distortions in the $p_{T,Z}$ distribution under variations of M_A are much less pronounced. The strong M_H -dependence of the E_T^{miss} spectrum in $h + E_T^{\text{miss}}$ production can be traced back to the structure of the coupling g_{Aha} . From (3.3) one sees that for smaller M_H also g_{Aha} is smaller, leading to a reduced $A \rightarrow ha$ branching ratio and in turn to a lower rate of resonant production. In contrast, the coupling g_{HZa} that drives resonant production in the case of the mono- Z signal does not depend on the value of M_A .

In order for resonant production to be dominant in both the $h + E_T^{\text{miss}}$ and $Z + E_T^{\text{miss}}$ case, we have chosen $M_H = M_A$ in the benchmark scenario (3.4). The further choice of a common 2HDM Higgs mass $M_H = M_A = M_{H^\pm}$ is motivated by the observation that such an option minimises the constraints from EW precision observables and vacuum stability. See the discussion in Section 3. While in our sensitivity studies presented in the next section we will always employ the choice $M_H = M_A = M_{H^\pm}$, in future 2HDM+a interpretations of mono- X searches one might however also want to consider cases with $M_H \neq M_A$. Kinematic distributions and cross-sections as a function of model parameters can be found in Appendix ??.

Variation of $\sin\theta$

Figure 13 shows E_T^{miss} distributions in $h + E_T^{\text{miss}}$ production (left panel) and $p_{T,Z}$ distributions in $Z + E_T^{\text{miss}}$ production (right panel) for different values of $\sin\theta$. The spin-0 masses are chosen as $M_H = M_A = M_{H^\pm} = 700$ GeV and $M_a = 400$ GeV, and the remaining

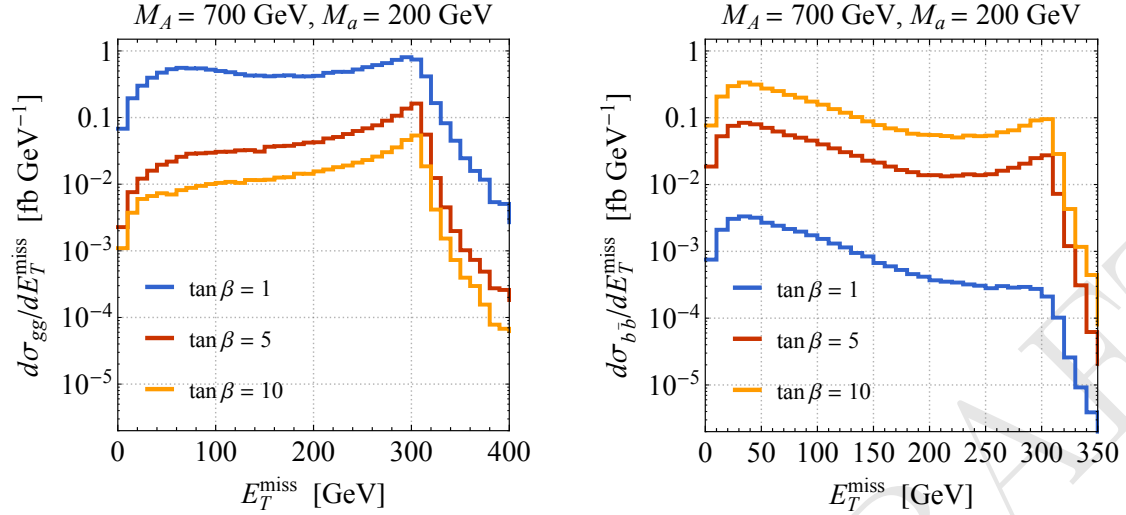


Figure 14: E_T^{miss} distributions for mono-Higgs production in gg -fusion (left panel) and $b\bar{b}$ -fusion (right panel) in the 2HDM+a model. The displayed results correspond to pp collisions at 13 TeV and different choices of $\tan\beta$. The parameters not detailed in the plots are set to (3.4) using $M_H = M_A = M_{H^\pm} = 700$ GeV and $M_a = 200$ GeV.

parameters are fixed to (3.4). From the two panels it is evident that a variation of $\sin\theta$ leads to both a rate and shape change in the case of the mono-Higgs signal, while in the case of the mono- Z channel only the total cross section gets rescaled to first approximation. The strong sensitivity of the shape of the E_T^{miss} spectrum in $h + E_T^{\text{miss}}$ production is again a result of the interplay of resonant and non-resonant contributions. While the $gg \rightarrow A \rightarrow ha \rightarrow h\chi\bar{\chi}$ amplitude scales as $\sin\theta \cos^3\theta$, the $gg \rightarrow ha \rightarrow h\chi\bar{\chi}$ matrix element shows a $\sin\theta \cos\theta$ dependence. These scalings imply that at small (large) $\sin\theta$ the resonant (non-resonant) amplitudes provide the dominant contribution to the E_T^{miss} distribution in mono-Higgs production. In the case of the mono- Z signal the resonant and non-resonant amplitudes both scale as $\sin\theta \cos\theta$ and in consequence the cross section and all kinematic distributions are essentially not distorted under changes of the mixing angle θ . Notice that the latter statement also holds in the case of the $t\bar{t} + E_T^{\text{miss}}$, $b\bar{b} + E_T^{\text{miss}}$ and mono-jet signatures. This can be deduced from (5.5).

From the above discussion it follows that the choice $\sin\theta = 0.35$ made in (3.4) leads to an enhanced sensitivity of the mono-Higgs signal to the 2HDM+a parameter space. To perform parameter scans in scenarios with larger mixing angles like $\sin\theta = 0.7$ would however also be worthwhile because such a choice would lead to an improved coverage via the mono- Z channel. We finally note that in scenarios with $\sin\theta > 0.35$ the maximal allowed size of mass splitting $M_H - M_a$ is more constrained by vacuum stability arguments than in (3.4). This can be seen from (3.2).

Variation of $\tan\beta$

In Figure 14 we display E_T^{miss} distributions in mono-Higgs production for different choices of $\tan\beta$. The left (right) panel illustrates the contributions from the $gg \rightarrow h + E_T^{\text{miss}}$

($b\bar{b} \rightarrow h + E_T^{\text{miss}}$) channel. The shown results have been obtained at 13 TeV and employ (3.4) with $M_H = M_A = M_{H^\pm} = 700$ GeV and $M_a = 200$ GeV. One first notices that the total production cross section in gg -fusion strongly decreases with increasing $\tan \beta$, while in the case of $b\bar{b}$ -fusion the opposite behaviour is observed. The strong depletion/enhancement of the production rates originates from the fact that in the type-II 2HDM+a model considered in this whitepaper the couplings of H, A, a to top quarks are proportional to $\cot \beta$, while the corresponding couplings to bottom quarks are proportional to $\tan \beta$. Numerically, we find that for $\tan \beta \gtrsim 5$ the gg -fusion and $b\bar{b}$ -fusion contributions to mono-Higgs production are comparable in size and thus both channels have to be included to obtain accurate predictions. From the two panels it is furthermore apparent that variations of $\tan \beta$ do not only change the overall signal strength, but also have a pronounced impact on the shapes of the E_T^{miss} distributions. In particular, changes in $\tan \beta$ influence the importance of resonant versus non-resonant contributions. Like in the case of the mono-Higgs channel also for the mono- Z signal $b\bar{b}$ -initiated production can be relevant for sufficiently large values of $\tan \beta$ [25]. [Uli: Show a plot here!] The modifications in the kinematic distributions of $t\bar{t} + E_T^{\text{miss}}$ and $j + E_T^{\text{miss}}$ production under changes of $\tan \beta$ are compared to the mono-Higgs and mono- Z signal less pronounced.

Our scans in the $M_a - M_H$ plane are based on the choice $\tan \beta = 1$, since for this value the existing mono-Higgs and mono- Z searches already allow to probe/exclude large regions in the mass planes. In future ATLAS and CMS analyses it would however be desirable that scans in $\tan \beta$ are carried out as well (cf. Section 7 and [25, 26, 33]). We add that in such a scan special attention has to be given to the fact that in the large- $\tan \beta$ limit the total decay widths of some of the Higgs states can become very large, potentially invalidating the NWA. [Caterina: add figure? or appendix?]

Variation of m_χ

The modifications of the $E_T^{\text{miss}}(p_{T,Z})$ spectrum in $h + E_T^{\text{miss}}$ ($Z + E_T^{\text{miss}}$) production under a variation of the DM mass m_χ are illustrated in the two panels of Figure 15. The given predictions correspond to pp collision at 13 TeV and employ the benchmark parameters (3.4) with $M_H = M_A = M_{H^\pm} = 700$ GeV and $M_a = 300$ GeV. One observes that the depicted scenarios with $M_a > 2m_\chi$ (green and purple histograms) lead to almost identical rates, E_T^{miss} and $p_{T,Z}$ spectra, while the choice $M_a < 2m_\chi$ (blue histograms) largely reduces the total rates and also modifies the shapes of the shown distributions. This feature is expected since for $M_a > m_\chi/2$ ($M_a < m_\chi/2$) the decay channel $a \rightarrow \chi\bar{\chi}$ is kinematically allowed (forbidden). In order to have detectable mono- X signals even for light mediators a , we have chosen a value of $m_\chi = 10$ GeV as the baseline for the following sensitivity studies. [Caterina: suggest a forward reference to the relic density]

6 Non- E_T^{miss} collider signatures

In this section we will discuss the most important non- E_T^{miss} signals that can be used to explore the parameter space of the 2HDM+a model at the LHC. Most of the discussion will be centred around final states containing top quarks since these channels provide the

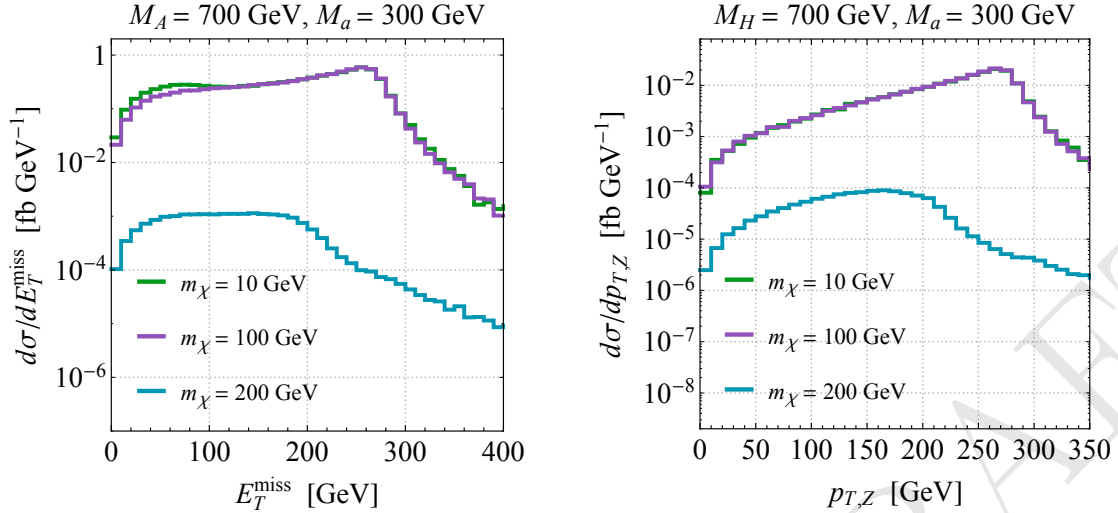


Figure 15: E_T^{miss} ($p_{T,Z}$) distributions for mono-Higgs (mono- Z) production at 13 TeV. The presented results correspond to different values of the DM mass m_χ . The other 2HDM+a parameters are set to (3.4) using $M_H = M_A = M_{H^\pm} = 700$ GeV and $M_a = 300$ GeV.

best sensitivity to model realisations with low $\tan\beta$ such as our benchmark parameter choice (3.4). Final states that give excess to the 2HDM+a parameter space with large $\tan\beta$ such as di-tau searches will however also be discussed briefly.

6.1 Di-top searches

In all 2HDM models, the spin-0 bosons H, A decay dominantly to top-quark pairs if these states have masses above the top-quark threshold, i.e. $M_{H,A} > 2m_t$, and if $\tan\beta = \mathcal{O}(1)$. New-physics scenarios of this kind can thus be tested by studying the $t\bar{t}$ invariant mass spectrum $m_{t\bar{t}}$. Interference effects between the signal process and the SM $t\bar{t}$ background however distort the $m_{t\bar{t}}$ signal shape from a single peak to a peak-dip structure [111–115], a feature that represents a serious obstacle to probe 2HDM models with $M_{H,A} > 350$ GeV and small $\tan\beta$ values [116–119].

The ATLAS search in Ref. [58] takes into account interference effects between the signal process $gg \rightarrow H/A \rightarrow t\bar{t}$ and the SM background $gg \rightarrow t\bar{t}$ is the . This search is based on an integrated luminosity of 20.3 fb^{-1} collected at 8 TeV and interprets results in the alignment limit of a type-II 2HDM without a pseudoscalar decaying to DM. The obtained exclusion limits in the $M_{H,A} - \tan\beta$ plane are stronger than previously published LHC constraints on the 2HDM parameter space with low $\tan\beta$ and $M_{H,A} \in [500, 650]$ GeV. For instance, for $M_{H,A} = 500$ GeV values of $\tan\beta < 1$ are disfavoured at 95% CL. A similar parameter space can be probed if the results [58] are reinterpreted in the context of the 2HDM+a model [25]. The di-top invariant mass spectra obtained in the 2HDM+a model as a function of different model parameters is shown in Figures 16 and 17.

[Uli: Work in progress!]

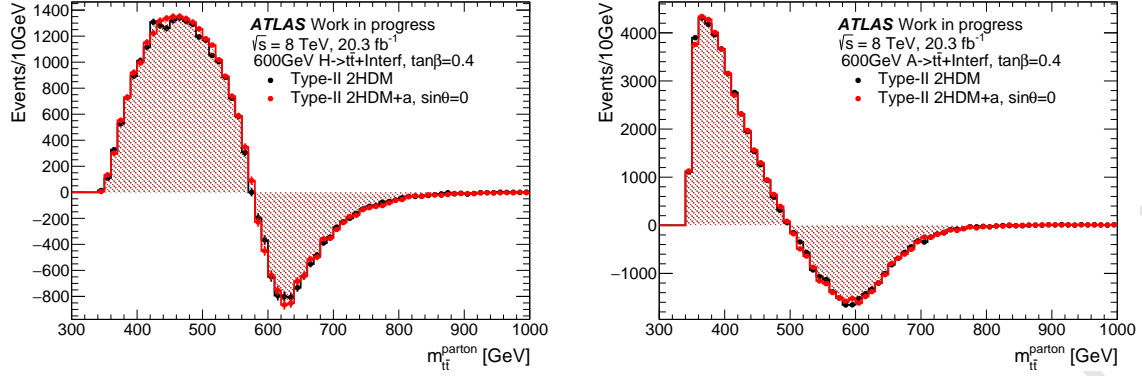


Figure 16: $m_{t\bar{t}}$ spectra for $gg \rightarrow H \rightarrow t\bar{t}$ (left) and $gg \rightarrow A \rightarrow t\bar{t}$ (right). The black (red) predictions correspond to the type-II 2HDM (2HDM+a) model. The shown results employ $M_A = M_H = 600$ GeV, $M_a = 100$ GeV, $\tan \beta = 0.4$ and $\sin \theta = 0$. [Uli: Fix notation etc.!]

A similar kinematic range could be probed if the result were re-interpreted in the context of the 2HDM+a. Interference between a loop-induced and a tree-level process cannot currently be simulated in MADGRAPH 5. To amend this problem, the same "Higgs_Effective_Couplings_FormFactor" approach [120] as adopted in [58] is implemented in the UFO, replacing the loop production by an effective vertex. The predictions of the modified UFO for the case, in which the pseudoscalar mediator does not mix with the heavy pseudoscalar A ($\sin \theta = 0$), i.e. effectively decouples from the 2HDM Higgs sector, are compared to those for the minimal 2HDM. Excellent agreement is found in the invariant mass distributions of A/H decaying into a top pair are shown in Fig. 16. As examples of how the sensitivity changes as a function of the parameters of the 2HDM+a, the $M_{t\bar{t}}$ distributions of pseudoscalars decaying into $t\bar{t}$ are presented in Fig 17. Larger values of $\tan \beta$ or $\sin \theta$ are expected to yield lower sensitivities to $A \rightarrow t\bar{t}$ significantly while M_a almost only affects the contribution from $a \rightarrow t\bar{t}$, which becomes sizeable if M_a is close to $2M_t$.

6.2 Four-top searches

The topology involving four top-quarks in the final state is a rare, yet increasingly important signature, which will gain sensitivity and attention with the enlargement of the dataset delivered by the LHC. In the attempt to perform a first characterisation of this topology, we have studied the predicted cross-section for the four top final state of this model for two sets of parameter choices.

In Figure 18a we present the four top cross section for the parameter choices for the parameter choices of $\sin \theta = 0.35$, $M_A = M_H = M_{H^\pm} = 600$ GeV, for an intermediate choice of mass of the light pseudoscalar ($m(a) = 400$ GeV), as a function of $\tan \beta$. [Caterina: this may be too technical?] The total four-top production cross section, which accounts for both SM and new physics (NP) contributions and is indicated as $|SM + NP|^2$ in the legend, is compared with the production cross section contributions separately due to SM and NP terms. This is achieved technically by setting a requirement on the number of QCD and

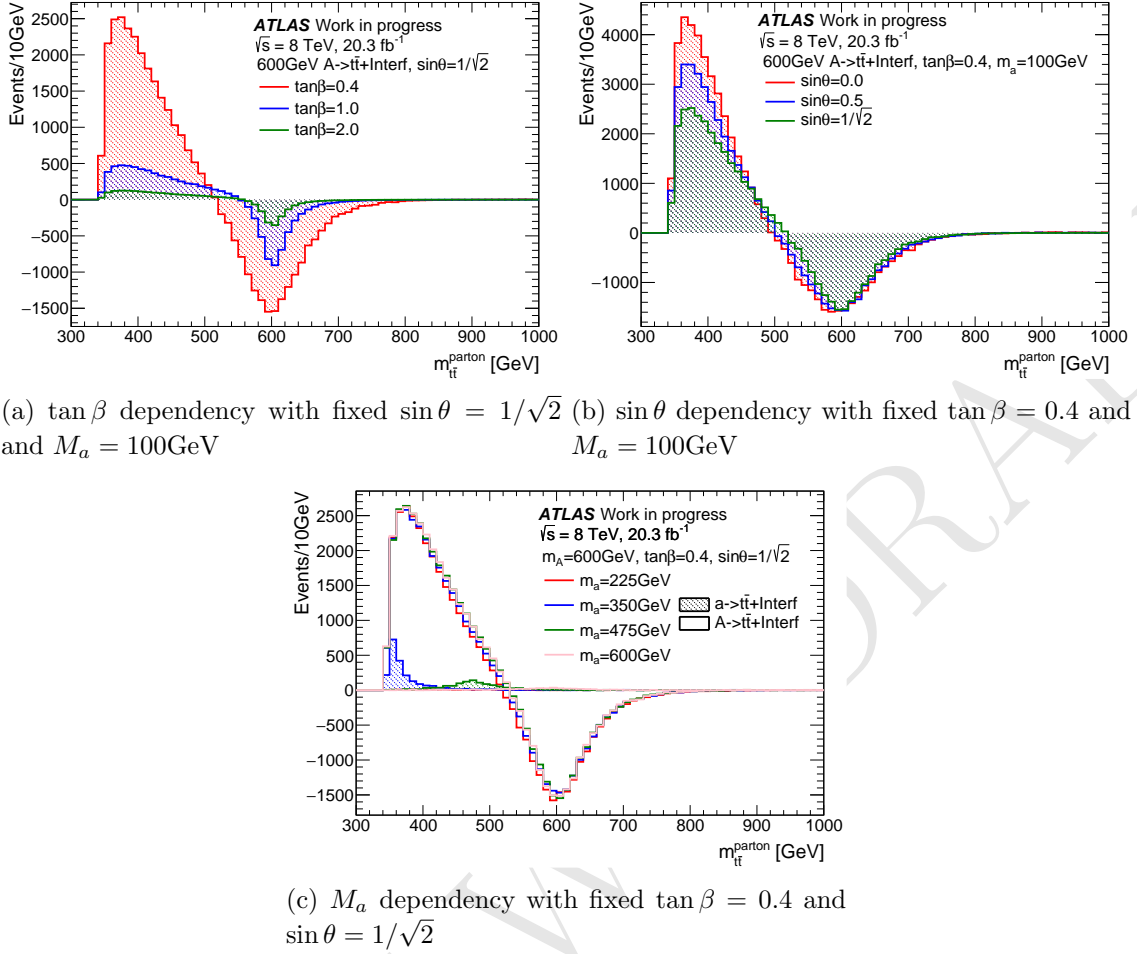


Figure 17: parameter dependency of signal $M_{\bar{t}t}$ distribution mediated by pseudoscalars. The value of M_A is fixed at 600GeV.

QED vertices in madgraph, as indicated in Table 1. The dominant contribution is driven by the on-shell production of A and H for all choices of $\tan\beta$ in this benchmark. In the lower panel of Figure 18a, the effect of the interference term between the 2HDM+ a and the SM is assessed, and is found to have an impact almost always smaller than 5% on the inclusive cross-section. We note however that the validity of this statement depends on the selection in the experimental analysis.

[Caterina: clarify what benchmark 3a and 3b are in the following?] In Figure 18b we present the cross-section study when using $\sin\theta = \frac{1}{\sqrt{2}}$, as a function of the light pseudoscalar mass. For these parameter choices the cross-section is independent of $m(a)$. As it can be observed from the on-shell contribution breakdown, at the low-end of the mass spectrum the $\bar{t}t + a$ production dominates, with a peak at 400 GeV due to the competition between $a \rightarrow \chi\chi$ and $a \rightarrow \bar{t}t$ and the decreasing of the cross section with the increase of $m(a)$. The contribution of $\bar{t}t + H$ and $\bar{t}t + A$ processes compensates the latter effect in the higher end of the mass-spectrum, with the turn on starting around 800 GeV due to

MADGRAPH rule	Legend symbol	Details
$p p > t \bar{t} t \bar{t} / a z h1 \text{ QED} \leq 2$	$ SM + NP ^2$	Four-top production including both SM and NP contributions and their interference.
$p p > t \bar{t} t \bar{t} / a z h1 \text{ QCD} \leq 2$	$ NP ^2$	Four-top production from NP processes, including interference terms among A, H, a .
$p p > t \bar{t} t \bar{t} / a z h1 \text{ QED} \leq 0$	$ SM ^2$	Four-top SM production.

Table 1: Description of the specific MADGRAPH settings used to derive the different curves of Figs 18a and 18b.

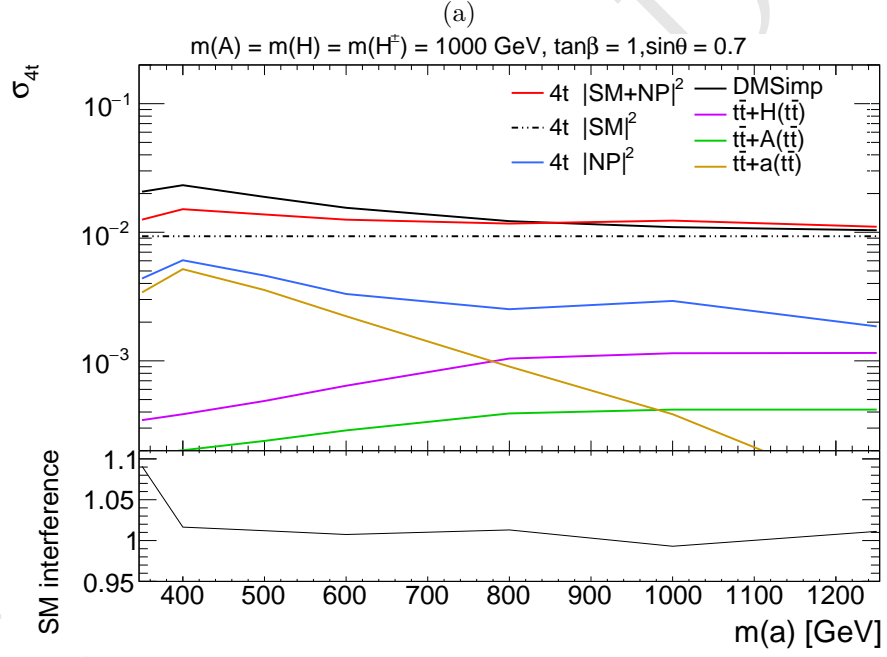
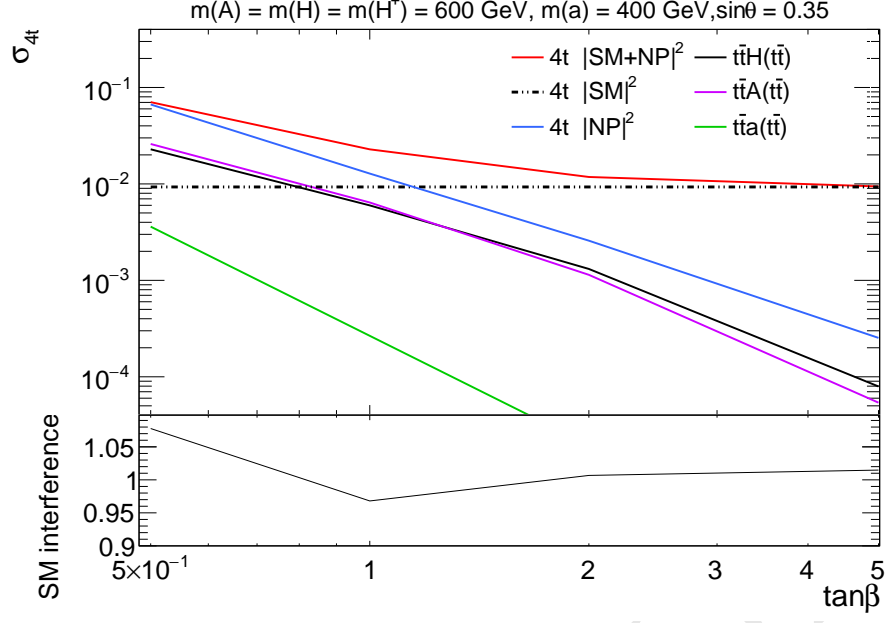
the competition between $A/H \rightarrow \bar{t}t$ and cascade decays of the heavy higgses into the light pseudoscalar mediator ($A \rightarrow ah/H \rightarrow aZ$). The small feature at 1 TeV is due to interference effects between the three higgs mediators, which are all set to the same mass for this parameter choice. The inclusive production cross-section of the 2HDM+a model is also compared with the one obtained by the **DMSimp** pseudoscalar implementation. Similarly to the previous benchmark points, the impact of the SM interference term on the inclusive cross-section is found to be very small ($< 2\%$), except for $m(a)$ values close to the top threshold.

Finally, in Figure 19 we compare for a small $\tan\beta$ value, the cross section of four-top production from NP processes (see Tab. 1) of benchmarks #3a and #3b. This cross-section increases for benchmark #3b for increasing $\sin\theta$, as the production mechanism is dominated by $\bar{t}t + a(\bar{t}t)$. A different and more flat trend is instead observed for benchmark #3a, for which the $\sin\theta$ dependence is more complex and driven by the branching ratios of A and H in a top pair, as the $a \rightarrow \bar{t}t$ threshold is closed in this case.

6.3 Other final states

7 Sensitivity studies

In this section we present sensitivity estimates for two of the main E_T^{miss} signatures in the 2HDM+a model, namely the $h + E_T^{\text{miss}}$ and the $Z + E_T^{\text{miss}}$ channels. Specifically, we will consider the mono-Higgs (mono- Z) signal in the $b\bar{b}$ ($\ell^+\ell^-$) channel. Our studies are based on generator-level reinterpretation of existing results with 36 fb^{-1} of LHC data taken at $\sqrt{s} = 13 \text{ TeV}$. These results contain different amounts of public information. In the mono-Higgs case model-independent limits presented in [95] are used for the reinterpretation, while in the mono- Z case the sensitivity is estimated using generator-level information on the signal together with published background estimates [98]. The sensitivities that other E_T^{miss} searches provide are also briefly discussed below.



(b)

Figure 18: Four-top cross section study for a subset of the parameter space of benchmark #2 (top) and #3 (bottom). The different Standard Model (SM) and New Physics (NP) contributions with and without interference and the breakdown in terms of on-shell mediator production is presented, following the notation of Table 1.

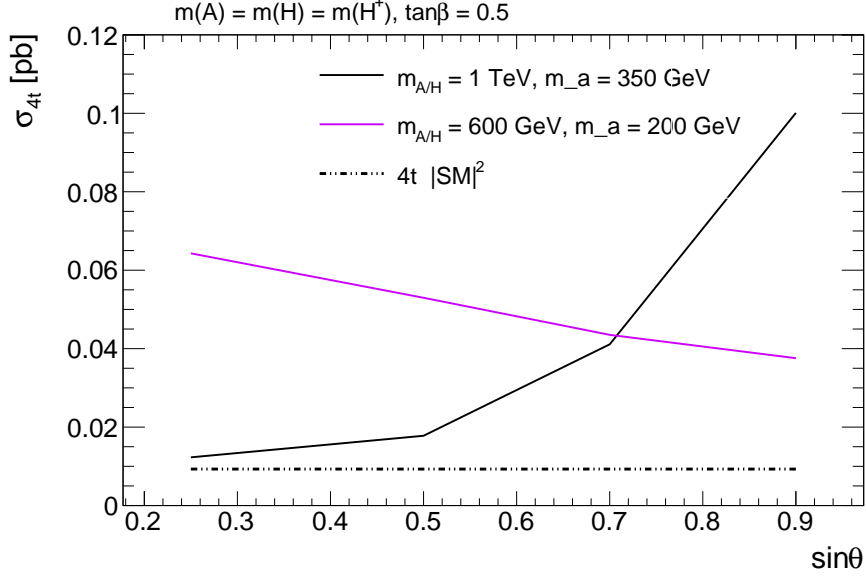


Figure 19: Four-top cross section comparison for benchmarks #3a and #3b. Only NP contribution is presented, following the notation of Table 1.

7.1 Mono-Higgs study

The sensitivity estimates of the ATLAS and CMS mono-Higgs searches in the $b\bar{b}$ channel to the 2HDM+a model are based on the model-independent limits on the anomalous production of the SM Higgs boson in association with E_T^{miss} derived in [95]. As these limits are set in terms of the observed production cross section of non-SM events with large E_T^{miss} and a Higgs boson, they can be compared directly to the cross sections obtained in the 2HDM+a model after taking into account the kinematic acceptance \mathcal{A} of the event selection and the detection efficiency ε . The variables of interest for the sensitivity study of the $b\bar{b} + E_T^{\text{miss}}$ searches are

$$S_i = \frac{\sigma_i(pp \rightarrow h + E_T^{\text{miss}})_{2\text{HDM}+a} \cdot \text{BR}(h \rightarrow b\bar{b})_{\text{SM}} \cdot (\mathcal{A} \cdot \varepsilon)_i}{\sigma_i(pp \rightarrow h + E_T^{\text{miss}} \rightarrow b\bar{b} + E_T^{\text{miss}})_{\text{obs}}}, \quad (7.1)$$

where $\sigma_i(pp \rightarrow h + E_T^{\text{miss}})_{2\text{HDM}+a}$ is the partonic cross section of the 2HDM+a signal, the branching ratio of the SM Higgs boson is denoted by $\text{BR}(h \rightarrow b\bar{b})_{\text{SM}} \simeq 58\%$ and $\sigma_i(pp \rightarrow h + E_T^{\text{miss}} \rightarrow b\bar{b} + E_T^{\text{miss}})_{\text{obs}}$ represents the observed upper cross-section limit on $h + E_T^{\text{miss}}$ production with $h \rightarrow b\bar{b}$. The cross sections as well as the product $\mathcal{A} \cdot \varepsilon$ depend on the considered E_T^{miss} bin as indicated by the index i . A particular point in parameter space is excluded if the sum $S = \sum_i S_i$ of the individual sensitivities is larger than 1.

The results of the sensitivity study for the mono-Higgs signal in the $b\bar{b}$ decay channel are shown in Figure 20. The upper panel in the figure displays S as a function of M_a and M_A . The observed cross-section limits $\sigma_i(pp \rightarrow h + E_T^{\text{miss}} \rightarrow b\bar{b} + E_T^{\text{miss}})_{\text{obs}}$ as well as the products $(\mathcal{A} \cdot \varepsilon)_i$ that enter (7.1) are taken from the recent ATLAS study [95]. One observes that the existing mono-Higgs searches allow to probe/exclude 2HDM+a scenarios

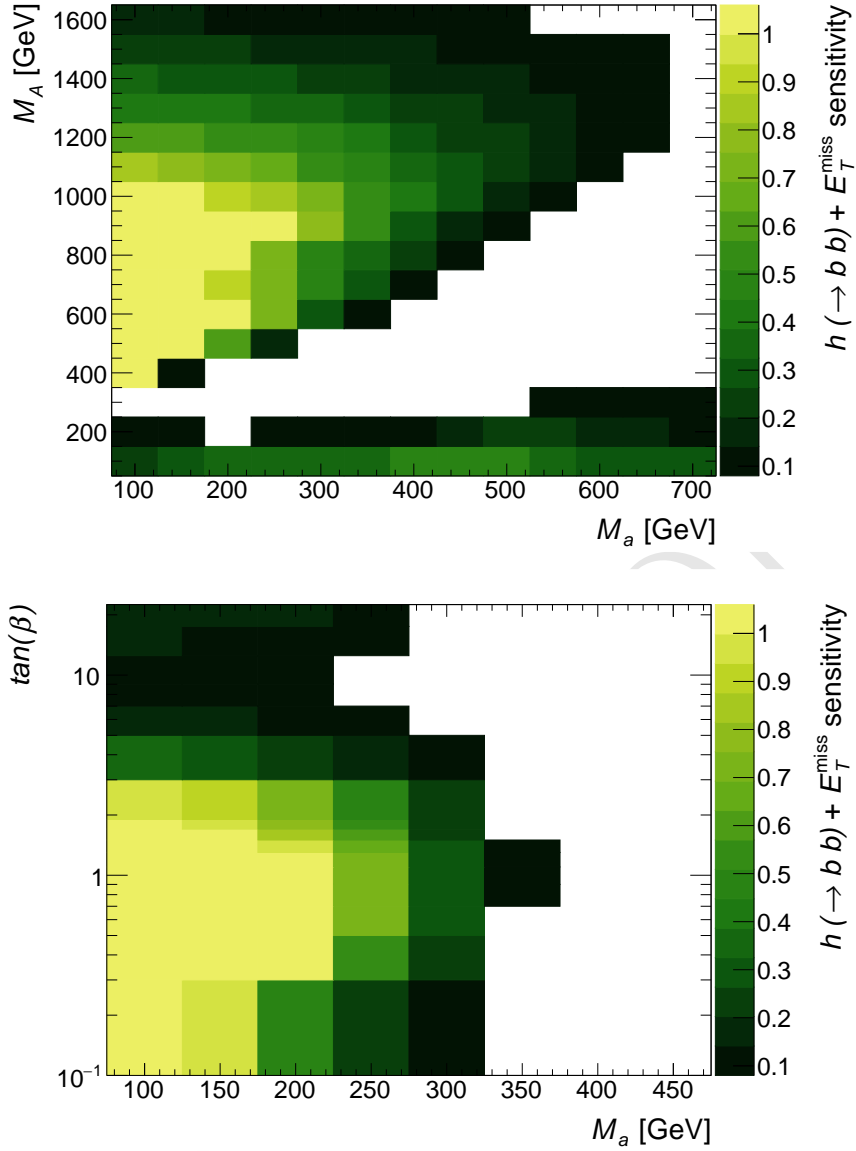


Figure 20: Estimated sensitivities of the $h + E_T^{\text{miss}}$ signature in the $h \rightarrow b\bar{b}$ channel. The upper (lower) panel shows our results in the M_a – M_A (M_a – $\tan\beta$) plane. **The remaining parameters are set to (3.4) in the upper panel, while in the lower panel $\tan\beta$ is left to vary but the common 2HDM Higgs mass is fixed to (3.5).** Bins with no content have a negligible sensitivity. See text for further explanations. [Uli: Use the same notation etc. for the plots in Figures 20 and 21!]

with $M_A > M_h + M_a$ and sufficiently small M_a values, while they are only weakly sensitive to models where the mass hierarchy between A and a is reversed, i.e. $M_a > M_h + M_A$. Numerically, we find that for a light a with $M_a \simeq 100$ GeV one has $S > 1$ for all values $M_A \simeq [350, 1050]$ GeV. Notice that in the parameter region $M_A > M_h + M_a$ the strong sensitivity of the search arises because the mono-Higgs signature is resonantly produced

via $pp \rightarrow A \rightarrow ha \rightarrow h\chi\bar{\chi}$ — see the discussion in Section 5.1. The sensitivity of the search decreases for increasing (decreasing) M_A because the production rate of $pp \rightarrow A$ decreases (the Jacobian peak (5.2) is shifted to lower E_T^{miss} values). In the region $M_a > M_h + M_A$, the largest contribution to the $h + E_T^{\text{miss}}$ cross section again originates from resonant production, namely $pp \rightarrow a \rightarrow hA \rightarrow h\chi\bar{\chi}$. The resulting sensitivities are however compared to the case discussed before much smaller because $\sigma(pp \rightarrow a)/\sigma(pp \rightarrow A) = \sin^2\theta/\cos^2\theta \simeq 1/7$, $\text{BR}(a \rightarrow Ah)/\text{BR}(A \rightarrow ah) < 1$ and $\text{BR}(A \rightarrow \chi\bar{\chi})/\text{BR}(a \rightarrow \chi\bar{\chi}) \ll 1$ for the parameter choices made in (3.4).

The lower panel in Figure 20 shows the sensitivity S in the M_a – $\tan\beta$ plane fixing M_H, M_A and M_{H^\pm} to (3.5). One observes that the existing mono-Higgs searches allow to exclude $\tan\beta \lesssim 3$ for $m_a \simeq 100$ GeV and $\tan\beta \lesssim 1$ for $m_a \lesssim 225$ GeV. From Figure 14 it is apparent that for such small values of $\tan\beta$, the $h + E_T^{\text{miss}}$ signal is dominantly produced through top-quark loops in gg -fusion. The corresponding production rate scales as $\sigma(gg \rightarrow A) \propto \cot^2\beta$, and as a result the sensitivity rapidly decreases for $\tan\beta > 1$. Notice that the decrease is to some extent counteracted by the fact that the Jacobian peak becomes more pronounced when $\tan\beta$ is increased (cf. the left panel in Figure 14). Another feature that is visible in the lower panel in Figure 20 is that at $\tan\beta \gtrsim 10$ the sensitivity of the mono-Higgs search starts to increase again, because the $b\bar{b}$ -initiated production cross section behaves like $\sigma(b\bar{b} \rightarrow A) \propto \tan^2\beta$. Further plots of our mono-Higgs sensitivity study can be found in Appendix ??.

7.2 Mono- Z study

In the absence of model-independent limits on anomalous production of $Z + E_T^{\text{miss}}$ events, the expected sensitivity of the mono- Z search to the 2HDM+a model is estimated by comparing the number of generator-level signal events to the number of expected background events. The published background predictions for $Z + E_T^{\text{miss}}$ production followed by $Z \rightarrow \ell^+\ell^-$ [98] are used which correspond to 36 fb^{-1} of 13 TeV data. The selection cuts and E_T^{miss} binnings that are applied to the signal events resemble those employed in the ATLAS analysis [98]. A reconstruction efficiency of 75% is assumed for signal events, and a conservative background systematic uncertainty of 20% (10%) is taken for events with $E_T^{\text{miss}} < 120$ GeV ($E_T^{\text{miss}} > 120$ GeV). Following the Asimov approximation, the significance $Z_{A,i}$ for individual bins i is calculated as a Poisson ratio of likelihoods modified to incorporate systematic uncertainties on the background. Explicitly one has [121]

$$Z_{A,i} = \sqrt{2 \left((s+b) \ln \left[\frac{(s+b)(b+\sigma_b^2)}{b^2 + (s+b)\sigma_b^2} \right] - \frac{b^2}{\sigma_b^2} \ln \left[1 + \frac{\sigma_b^2 s}{b(b+\sigma_b^2)} \right] \right)}, \quad (7.2)$$

where s (b) represents the expected number of signal (background) events and σ_s (σ_b) denotes the corresponding standard deviation that characterises systematic uncertainties. The total significance Z_A is then defined by adding the individual $Z_{A,i}$ in quadrature. The ATLAS and CMS experiments are expected to be sensitive to regions with total significances of $Z_A > 2$.

The results of our sensitivity study for the mono- Z signature in the $\ell^+\ell^-$ channel are presented in Figure 21. The upper (lower) panel displays the total significance Z_A in the

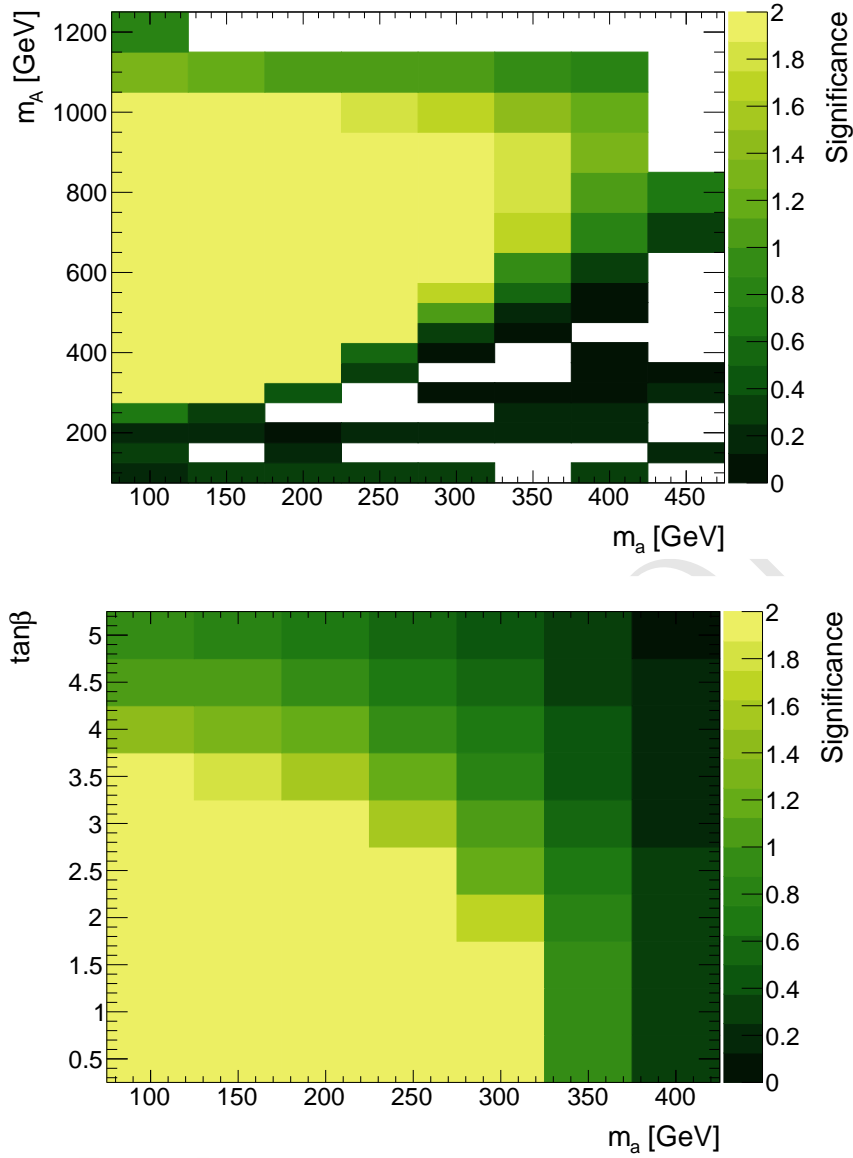


Figure 21: Estimated significance of the $Z + E_T^{\text{miss}}$ signature in the $Z \rightarrow \ell^+ \ell^-$ channel. The upper (lower) panel shows our results in the $M_a - M_A$ ($M_a - \tan \beta$) plane. The choice of parameters resembles those made in Figure 20. Further details can be found in the text. [Uli: Last statement correct? In particular, choice of $M_H = M_A = M_{H^\pm}$ in the case of the $M_a - \tan \beta$ plot has not been specified!]

$M_a - M_A$ ($M_a - \tan \beta$) plane. Comparing the obtained results to those depicted in Figure 20, one observes that for the parameter choices (3.4) the mono- Z and mono-Higgs searches allow to test quite similar parameter regions in the $M_a - M_A$ plane. Numerically, we find that for $M_a \simeq 100$ GeV the existing $Z + E_T^{\text{miss}}$ searches are sensitive to 2HDM pseudoscalar masses in the range of $M_A \simeq [300, 1050]$ GeV. Notice that the mono- Z sensitivity to lower values of M_A is slightly better than the one found in the mono-Higgs case. This enhanced

sensitivity arises because for fixed M_A and M_a and given that $M_Z < M_h$ the endpoint $E_{T,\max}^{\text{miss}}$ of the E_T^{miss} distribution in $Z + E_T^{\text{miss}}$ production is always higher than that in the $h + E_T^{\text{miss}}$ channel. In contrast, in the parameter region with $M_a > M_Z + M_A$ the sensitivity of the mono- Z signature is weaker than that of the mono-Higgs signal. This feature is readily understood by noticing that the $pp \rightarrow a \rightarrow ZH$ channel does not lead to a E_T^{miss} signature, since the scalar H does not decay invisibly in the 2HDM+a model. For $M_a > M_Z + M_A$ hence only non-resonant diagrams contribute to the $Z + E_T^{\text{miss}}$ signature, and the sensitivity to such model realisations is consequently very weak.

In the lower panel of Figure 21 we plot the significance Z_A in the M_a - $\tan\beta$ plane for the choice (3.5). [Uli: Correct? Or other choice?] We see that present mono- Z searches are able to exclude $\tan\beta \lesssim 3.5$ for $m_a \simeq 100$ GeV and $\tan\beta \lesssim 1$ for $m_a \lesssim 325$ GeV. The quoted exclusion limits compare favourable with the mono-Higgs case. We add that in models where the bottom-quark Yukawa coupling is $\tan\beta$ enhanced such as the type-II scenario studied here, $b\bar{b} \rightarrow Z + E_T^{\text{miss}}$ production starts to become relevant for $\tan\beta \gtrsim 10$ [25]. Since only gg -fusion but not $b\bar{b}$ -fusion production is included in our mono- Z simulations, only $\tan\beta$ values up to 5.5 are plotted in the lower panel of Figure 21. Further details on our mono- Z sensitivity study are given in Appendix ??.

7.3 Sensitivity of other mono- X channels

The sensitivities of the LHC to the associated production of DM with a single top has been studied in the framework of the 2HDM+a model in [26]. This analysis assumes 300 fb^{-1} of data and finds that the $tX + E_T^{\text{miss}}$ signatures complement the parameter space coverage of the mono-Higgs and mono- Z signals considered by us in detail. Since searches for associated production of DM with a single top have so far not been performed at the LHC, one cannot use existing model-independent limits to estimate the sensitivity of these channels. For this reason we do not perform a sensitivity study of the $tX + E_T^{\text{miss}}$ signatures in this whitepaper.

Sensitivity studies of the $t\bar{t} + E_T^{\text{miss}}$ and $j + E_T^{\text{miss}}$ channels in the 2HDM+a have been performed in [25]. The results presented in that work imply that for the benchmark parameter choices (3.4), the latest $t\bar{t} + E_T^{\text{miss}}$ and mono-jet searches that are based on 36 fb^{-1} of 13 TeV data have only a very weak sensitivity to the parameter space shown in Figures 20 and 21. Given the weak sensitivity of the $t\bar{t} + E_T^{\text{miss}}$ and $j + E_T^{\text{miss}}$ modes we do not perform sensitivity studies for these channels in this whitepaper. The $b\bar{b} + E_T^{\text{miss}}$ channel is also not considered here due to the same reason. Notice however that a reinterpretation of existing $t\bar{t} + E_T^{\text{miss}}$, $b\bar{b} + E_T^{\text{miss}}$ and $j + E_T^{\text{miss}}$ results is straightforward by using the general rescaling strategy discussed in Appendix A.

A Recasting procedure

In this appendix we discuss a general strategy that can be used to reinterpret existing $t\bar{t} + E_T^{\text{miss}}$, $b\bar{b} + E_T^{\text{miss}}$ and $j + E_T^{\text{miss}}$ results obtained in the DMF pseudoscalar model in terms of the 2HDM+a model. Example diagrams that lead to these mono- X signatures in the

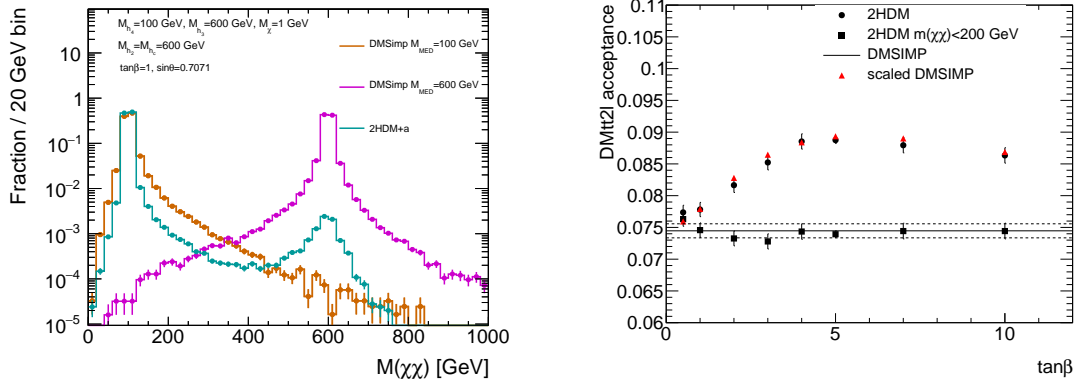


Figure 22: Left: Invariant mass of the $\chi\bar{\chi}$ system in $t\bar{t} + E_T^{\text{miss}}$ production for the DMF pseudoscalar model with $M_a = 100$ GeV (brown) and $M_a = 600$ GeV (magenta) compared to the 2HDM+a model with $M_a = 100$ GeV, $M_H = M_A = M_{H^\pm} = 600$ GeV, $\sin\theta = 0.7071$ and $\tan\beta = 1$ (cyan). Right: Acceptances of the two-lepton $t\bar{t} + E_T^{\text{miss}}$ analysis [106] as a function of $\tan\beta$. Shown are the predictions in the 2HDM+a model without (round black markers) and with the cut $m_{\chi\bar{\chi}} < 200$ GeV (square black markers), assuming $M_a = 150$ GeV, $M_H = M_A = M_{H^\pm} = 600$ GeV and $\sin\theta = 0.35$. The DMF pseudoscalar model result (full black line) with its statistical uncertainty (dashed black lines) as well as the acceptance $\mathcal{A}_{2\text{HDM}+a}(M_a, M_A)$ (red triangles) as defined in (A.1) is also depicted. [Uli: Fix notation etc.!]

2HDM+a model are displayed Figure 10. Notice that only graphs involving the exchange of an a are depicted in this figure but similar diagrams with an A are not explicitly shown.

The relevance of the contributions from both the a and A in the 2HDM+a model can be nicely demonstrated by considering the invariant mass $m_{\chi\bar{\chi}}$ of the $\chi\bar{\chi}$ system. Examples of $m_{\chi\bar{\chi}}$ distributions in $t\bar{t} + E_T^{\text{miss}}$ production are shown in the left panel of Figure 22. The brown (magenta) histogram corresponds to the prediction in the DMF pseudoscalar model assuming a mediator mass of $M_a = 100$ GeV ($M_a = 600$ GeV), while the cyan histogram illustrates the result in the 2HDM+a model for the choices $M_a = 100$ GeV, $M_H = M_A = M_{H^\pm} = 600$ GeV, $\sin\theta = 0.7071$ and $\tan\beta = 1$. One observes that the predictions obtained in the DMF pseudoscalar model both show a single Breit-Wigner peak at $m_{\chi\bar{\chi}} = M_a$, which corresponds to the on-shell production of the mediator a that subsequently decays to a pair of DM particles. The 2HDM+a result instead features two mass peaks, one at $m_{\chi\bar{\chi}} = M_a$ and another one at $m_{\chi\bar{\chi}} = M_A$, because both pseudoscalars can be produced on-shell and then decay invisibly via either $a \rightarrow \chi\bar{\chi}$ or $A \rightarrow \chi\bar{\chi}$.

The above discussion suggests that once the contributions from a and A production are separated, $t\bar{t} + E_T^{\text{miss}}$, $b\bar{b} + E_T^{\text{miss}}$ and $j + E_T^{\text{miss}}$ results obtained in the DMF pseudoscalar model can be mapped into the 2HDM+a parameter space. In practice, the remapping is achieved by calculating the selection acceptances $\mathcal{A}_{\text{DMF}}(M_a)$ and $\mathcal{A}_{\text{DMF}}(M_A)$ in the DMF pseudoscalar model and the respective cross sections $\sigma_{a,\text{DMF}}$ and $\sigma_{A,\text{DMF}}$. The acceptance $\mathcal{A}_{2\text{HDM}+a}(M_a, M_A)$ in the 2HDM+a model is then obtained by computing the

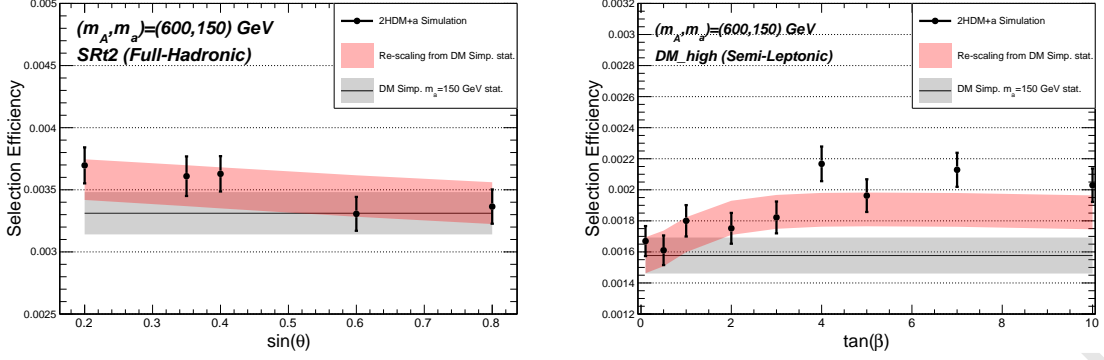


Figure 23: Validation of (A.1) in the case of the hadronic (left panel) and the one-lepton (right panel) final state arising from the $t\bar{t} + E_T^{\text{miss}}$ signature. The direct 2HDM+a calculations are indicated by the black dots and error bars, while the grey and red bands indicate the result in the DMF pseudoscalar model and the prediction obtained using the rescaling formula. In the left (right) panel, the chosen parameters are $M_a = 150$ GeV, $M_H = M_A = M_{H^\pm} = 600$ GeV and $\tan\beta = 1$ ($\sin\theta = 0.35$). [Uli: Correct? Fix notation etc.!]

following weighted average

$$\mathcal{A}_{2\text{HDM}+a}(M_a, M_A) = \frac{\mathcal{A}_{\text{DMF}}(M_a) \sigma_{a,\text{DMF}} + \mathcal{A}_{\text{DMF}}(M_A) \sigma_{A,\text{DMF}}}{\sigma_{a,\text{DMF}} + \sigma_{A,\text{DMF}}}. \quad (\text{A.1})$$

In the right panel of Figure 22 we show the results that are obtained by applying the latter equation to a parton-level implementation of the two-lepton $t\bar{t} + E_T^{\text{miss}}$ analysis described in [106]. The round (square) black markers indicate the results of a direct calculation in the 2HDM+a model without a $m_{\chi\bar{\chi}}$ cut (imposing the cut $m_{\chi\bar{\chi}} < 200$ GeV), using $M_a = 150$ GeV, $M_H = M_A = M_{H^\pm} = 600$ GeV and $\sin\theta = 0.35$. The DMF pseudoscalar model result with its statistical uncertainty is represented by the solid and dashed black lines. The acceptance calculated from (A.1) is finally indicated by the red triangles. Two features are evident from the figure. First, the 2HDM+a acceptance with cut agrees with uncertainties with the acceptance of the DMF pseudoscalar model. This is expected because the cut $m_{\chi\bar{\chi}} < 200$ GeV strongly suppresses the A contribution in the 2HDM+a model. Second, the acceptance estimated using (A.1) agrees within uncertainties with the acceptance evaluated directly in the 2HDM+a sample.

Further validations of (A.1) are presented in Figure 23. In this figure we apply the rescaling formula to the case of the hadronic [106] (left panel) and the one-lepton [122] (right panel) final state arising in the context of $t\bar{t} + E_T^{\text{miss}}$ production. The direct 2HDM+a calculations are indicated by the black dots and error bars, while the grey and red bands illustrate the result in the DMF pseudoscalar model and the prediction obtained using (A.1). In the left (right) panel, we have employed $M_a = 150$ GeV, $M_H = M_A = M_{H^\pm} = 600$ GeV and $\tan\beta = 1$ ($\sin\theta = 0.35$). One observes that the rescaled results describe the $\sin\theta$ and

$\tan\beta$ dependence of the 2HDM+a result well. [Uli: In fact, not an amazing agreement!] We finally add that the formula (A.1) has also been successfully tested in the case that $|M_A - M_a| \simeq 50 \text{ GeV}$, in which case the interference between the a and A contributions is phenomenologically relevant.

References

- [1] Q.-H. Cao, C.-R. Chen, C. S. Li, and H. Zhang, *Effective Dark Matter Model: Relic density, CDMS II, Fermi LAT and LHC*, *JHEP* **1108** (2011) 018, [[arXiv:0912.4511](#)].
- [2] M. Beltran, D. Hooper, E. W. Kolb, Z. A. Krusberg, and T. M. Tait, *Maverick dark matter at colliders*, *JHEP* **1009** (2010) 037, [[arXiv:1002.4137](#)].
- [3] J. Goodman, M. Ibe, A. Rajaraman, W. Shepherd, T. M. Tait, et al., *Constraints on Light Majorana dark Matter from Colliders*, *Phys.Lett.* **B695** (2011) 185–188, [[arXiv:1005.1286](#)].
- [4] Y. Bai, P. J. Fox, and R. Harnik, *The Tevatron at the Frontier of Dark Matter Direct Detection*, *JHEP* **1012** (2010) 048, [[arXiv:1005.3797](#)].
- [5] J. Goodman, M. Ibe, A. Rajaraman, W. Shepherd, T. M. Tait, et al., *Constraints on Dark Matter from Colliders*, *Phys.Rev.* **D82** (2010) 116010, [[arXiv:1008.1783](#)].
- [6] P. J. Fox, R. Harnik, J. Kopp, and Y. Tsai, *Missing Energy Signatures of Dark Matter at the LHC*, *Phys. Rev.* **D85** (2012) 056011, [[arXiv:1109.4398](#)].
- [7] P. J. Fox, R. Harnik, J. Kopp, and Y. Tsai, *LEP Shines Light on Dark Matter*, *Phys.Rev.* **D84** (2011) 014028, [[arXiv:1103.0240](#)].
- [8] I. M. Shoemaker and L. Vecchi, *Unitarity and Monojet Bounds on Models for DAMA, CoGeNT, and CRESST-II*, *Phys. Rev.* **D86** (2012) 015023, [[arXiv:1112.5457](#)].
- [9] G. Busoni, A. De Simone, E. Morgante, and A. Riotto, *On the Validity of the Effective Field Theory for Dark Matter Searches at the LHC*, *Phys. Lett.* **B728** (2014) 412–421, [[arXiv:1307.2253](#)].
- [10] O. Buchmuller, M. J. Dolan, and C. McCabe, *Beyond Effective Field Theory for Dark Matter Searches at the LHC*, *JHEP* **01** (2014) 025, [[arXiv:1308.6799](#)].
- [11] G. Busoni, A. De Simone, J. Gramling, E. Morgante, and A. Riotto, *On the Validity of the Effective Field Theory for Dark Matter Searches at the LHC, Part II: Complete Analysis for the s-channel*, *JCAP* **1406** (2014) 060, [[arXiv:1402.1275](#)].
- [12] G. Busoni, A. De Simone, T. Jacques, E. Morgante, and A. Riotto, *On the Validity of the Effective Field Theory for Dark Matter Searches at the LHC Part III: Analysis for the t-channel*, *JCAP* **1409** (2014) 022, [[arXiv:1405.3101](#)].
- [13] D. Racco, A. Wulzer, and F. Zwirner, *Robust collider limits on heavy-mediator Dark Matter*, *JHEP* **05** (2015) 009, [[arXiv:1502.04701](#)].
- [14] S. Bruggisser, F. Riva, and A. Urbano, *The Last Gasp of Dark Matter Effective Theory*, *JHEP* **11** (2016) 069, [[arXiv:1607.02475](#)].
- [15] S. Bruggisser, F. Riva, and A. Urbano, *Strongly Interacting Light Dark Matter*, *SciPost Phys.* **3** (2017), no. 3 017, [[arXiv:1607.02474](#)].
- [16] J. Abdallah et al., *Simplified Models for Dark Matter Searches at the LHC*, *Phys. Dark Univ.* **9-10** (2015) 8–23, [[arXiv:1506.03116](#)].
- [17] D. Abercrombie et al., *Dark Matter Benchmark Models for Early LHC Run-2 Searches: Report of the ATLAS/CMS Dark Matter Forum*, [[arXiv:1507.00966](#)].
- [18] D. Curtin et al., *Exotic decays of the 125 GeV Higgs boson*, *Phys. Rev.* **D90** (2014), no. 7 075004, [[arXiv:1312.4992](#)].

- [19] U. Haisch, J. F. Kamenik, A. Malinauskas, and M. Spira, *Collider constraints on light pseudoscalars*, *JHEP* **03** (2018) 178, [[arXiv:1802.02156](#)].
- [20] N. F. Bell, Y. Cai, J. B. Dent, R. K. Leane, and T. J. Weiler, *Dark matter at the LHC: Effective field theories and gauge invariance*, *Phys. Rev.* **D92** (2015), no. 5 053008, [[arXiv:1503.07874](#)].
- [21] N. F. Bell, Y. Cai, and R. K. Leane, *Mono-W Dark Matter Signals at the LHC: Simplified Model Analysis*, *JCAP* **1601** (2016), no. 01 051, [[arXiv:1512.00476](#)].
- [22] U. Haisch, F. Kahlhoefer, and T. M. P. Tait, *On Mono-W Signatures in Spin-1 Simplified Models*, *Phys. Lett.* **B760** (2016) 207–213, [[arXiv:1603.01267](#)].
- [23] C. Englert, M. McCullough, and M. Spannowsky, *S-Channel Dark Matter Simplified Models and Unitarity*, *Phys. Dark Univ.* **14** (2016) 48–56, [[arXiv:1604.07975](#)].
- [24] D. Goncalves, P. A. N. Machado, and J. M. No, *Simplified Models for Dark Matter Face their Consistent Completions*, *Phys. Rev.* **D95** (2017), no. 5 055027, [[arXiv:1611.04593](#)].
- [25] M. Bauer, U. Haisch, and F. Kahlhoefer, *Simplified dark matter models with two Higgs doublets: I. Pseudoscalar mediators*, *JHEP* **05** (2017) 138, [[arXiv:1701.07427](#)].
- [26] P. Pani and G. Polesello, *Dark matter production in association with a single top-quark at the LHC in a two-Higgs-doublet model with a pseudoscalar mediator*, *Phys. Dark Univ.* **21** (2018) 8–15, [[arXiv:1712.03874](#)].
- [27] U. Haisch, F. Kahlhoefer, and J. Unwin, *The impact of heavy-quark loops on LHC dark matter searches*, *JHEP* **1307** (2013) 125, [[arXiv:1208.4605](#)].
- [28] P. J. Fox and C. Williams, *Next-to-Leading Order Predictions for Dark Matter Production at Hadron Colliders*, *Phys. Rev.* **D87** (2013) 054030, [[arXiv:1211.6390](#)].
- [29] M. R. Buckley, D. Feld, and D. Goncalves, *Scalar Simplified Models for Dark Matter*, *Phys. Rev.* **D91** (2015) 015017, [[arXiv:1410.6497](#)].
- [30] P. Harris, V. V. Khoze, M. Spannowsky, and C. Williams, *Constraining Dark Sectors at Colliders: Beyond the Effective Theory Approach*, *Phys. Rev.* **D91** (2015) 055009, [[arXiv:1411.0535](#)].
- [31] U. Haisch and E. Re, *Simplified dark matter top-quark interactions at the LHC*, *JHEP* **06** (2015) 078, [[arXiv:1503.00691](#)].
- [32] S. Ipek, D. McKeen, and A. E. Nelson, *A Renormalizable Model for the Galactic Center Gamma Ray Excess from Dark Matter Annihilation*, *Phys. Rev.* **D90** (2014), no. 5 055021, [[arXiv:1404.3716](#)].
- [33] J. M. No, *Looking through the pseudoscalar portal into dark matter: Novel mono-Higgs and mono-Z signatures at the LHC*, *Phys. Rev.* **D93** (2016), no. 3 031701, [[arXiv:1509.01110](#)].
- [34] P. Tunney, J. M. No, and M. Fairbairn, *Probing the pseudoscalar portal to dark matter via $\bar{b}bZ(\rightarrow \ell\ell) + \cancel{E}_T$: From the LHC to the Galactic Center excess*, *Phys. Rev.* **D96** (2017), no. 9 095020, [[arXiv:1705.09670](#)].
- [35] S. L. Glashow and S. Weinberg, *Natural Conservation Laws for Neutral Currents*, *Phys. Rev.* **D15** (1977) 1958.
- [36] E. A. Paschos, *Diagonal Neutral Currents*, *Phys. Rev.* **D15** (1977) 1966.
- [37] **ATLAS, CMS Collaboration**, G. Aad et al., *Measurements of the Higgs boson production and decay rates and constraints on its couplings from a combined ATLAS and CMS analysis*

of the LHC pp collision data at $\sqrt{s} = 7$ and 8 TeV, *JHEP* **08** (2016) 045, [[arXiv:1606.02266](#)].

- [38] J. F. Gunion and H. E. Haber, *The CP conserving two Higgs doublet model: The Approach to the decoupling limit*, *Phys. Rev.* **D67** (2003) 075019, [[hep-ph/0207010](#)].
- [39] T. Hermann, M. Misiak, and M. Steinhauser, $\bar{B} \rightarrow X_s \gamma$ in the Two Higgs Doublet Model up to Next-to-Next-to-Leading Order in QCD, *JHEP* **11** (2012) 036, [[arXiv:1208.2788](#)].
- [40] M. Misiak et al., *Updated NNLO QCD predictions for the weak radiative B-meson decays*, *Phys. Rev. Lett.* **114** (2015), no. 22 221801, [[arXiv:1503.01789](#)].
- [41] M. Misiak and M. Steinhauser, *Weak radiative decays of the B meson and bounds on M_{H^\pm} in the Two-Higgs-Doublet Model*, *Eur. Phys. J.* **C77** (2017), no. 3 201, [[arXiv:1702.04571](#)].
- [42] L. F. Abbott, P. Sikivie, and M. B. Wise, *Constraints on Charged Higgs Couplings*, *Phys. Rev.* **D21** (1980) 1393.
- [43] C. Q. Geng and J. N. Ng, *Charged Higgs Effect in B_d^0 - \bar{B}_d^0 Mixing, $K \rightarrow \pi$ Neutrino Anti-neutrino Decay and Rare Decays of B Mesons*, *Phys. Rev.* **D38** (1988) 2857. [Erratum: *Phys. Rev.* **D41**, 1715 (1990)].
- [44] A. J. Buras, P. Krawczyk, M. E. Lautenbacher, and C. Salazar, B^0 - \bar{B}^0 Mixing, CP Violation, $K^+ \rightarrow \pi^+ \nu \bar{\nu}$ and $B \rightarrow K \gamma X$ in a Two Higgs Doublet Model, *Nucl. Phys.* **B337** (1990) 284–312.
- [45] M. Kirk, A. Lenz, and T. Rauh, *Dimension-six matrix elements for meson mixing and lifetimes from sum rules*, *JHEP* **12** (2017) 068, [[arXiv:1711.02100](#)].
- [46] W. Skiba and J. Kalinowski, $B_s \rightarrow \tau^+ \tau^-$ decay in a two Higgs doublet model, *Nucl. Phys.* **B404** (1993) 3–19.
- [47] H. E. Logan and U. Nierste, $B_{s,d} \rightarrow \ell^+ \ell^-$ in a two Higgs doublet model, *Nucl. Phys.* **B586** (2000) 39–55, [[hep-ph/0004139](#)].
- [48] P. H. Chankowski and L. Slawianowska, $B_{d,s}^0 \rightarrow \mu^+ \mu^-$ decay in the MSSM, *Phys. Rev.* **D63** (2001) 054012, [[hep-ph/0008046](#)].
- [49] C. Bobeth, T. Ewerth, F. Krüger, and J. Urban, *Analysis of neutral Higgs boson contributions to the decays $\bar{B}_{(s)} \rightarrow \ell^+ \ell^-$ and $\bar{B} \rightarrow K \ell^+ \ell^-$* , *Phys. Rev.* **D64** (2001) 074014, [[hep-ph/0104284](#)].
- [50] C. Bobeth, M. Gorbahn, T. Hermann, M. Misiak, E. Stamou, and M. Steinhauser, $B_{s,d} \rightarrow l^+ l^-$ in the Standard Model with Reduced Theoretical Uncertainty, *Phys. Rev. Lett.* **112** (2014) 101801, [[arXiv:1311.0903](#)].
- [51] **LHCb, CMS Collaboration**, V. Khachatryan et al., *Observation of the rare $B_s^0 \rightarrow \mu^+ \mu^-$ decay from the combined analysis of CMS and LHCb data*, *Nature* **522** (2015) 68–72, [[arXiv:1411.4413](#)].
- [52] **LHCb Collaboration**, R. Aaij et al., *Measurement of the $B_s^0 \rightarrow \mu^+ \mu^-$ branching fraction and effective lifetime and search for $B^0 \rightarrow \mu^+ \mu^-$ decays*, *Phys. Rev. Lett.* **118** (2017), no. 19 191801, [[arXiv:1703.05747](#)].
- [53] A. Denner, R. J. Guth, W. Hollik, and J. H. Kühn, *The Z width in the two Higgs doublet model*, *Z. Phys.* **C51** (1991) 695–705.
- [54] U. Haisch and A. Weiler, *Determining the Sign of the Z^- Penguin Amplitude*, *Phys. Rev.* **D76** (2007) 074027, [[arXiv:0706.2054](#)].

- [55] A. Freitas and Y.-C. Huang, *Electroweak two-loop corrections to $\sin^2\theta_{eff}^{b\bar{b}}$ and R_b using numerical Mellin-Barnes integrals*, *JHEP* **08** (2012) 050, [[arXiv:1205.0299](#)]. [Erratum: *JHEP*10,044(2013)].
- [56] **ATLAS** Collaboration, M. Aaboud et al., *Search for additional heavy neutral Higgs and gauge bosons in the ditau final state produced in 36 fb¹ of pp collisions at $\sqrt{s} = 13$ TeV with the ATLAS detector*, *JHEP* **01** (2018) 055, [[arXiv:1709.07242](#)].
- [57] **CMS** Collaboration, A. M. Sirunyan et al., *Search for additional neutral MSSM Higgs bosons in the $\tau\tau$ final state in proton-proton collisions at $\sqrt{s} = 13$ TeV*, [arXiv:1803.06553](#).
- [58] **ATLAS** Collaboration, M. Aaboud et al., *Search for Heavy Higgs Bosons A/H Decaying to a Top Quark Pair in pp Collisions at $\sqrt{s} = 8$ TeV with the ATLAS Detector*, *Phys. Rev. Lett.* **119** (2017), no. 19 191803, [[arXiv:1707.06025](#)].
- [59] **ATLAS** Collaboration, M. Aaboud et al., *Search for pair production of up-type vector-like quarks and for four-top-quark events in final states with multiple b-jets with the ATLAS detector*, [arXiv:1803.09678](#).
- [60] H. E. Haber and A. Pomarol, *Constraints from global symmetries on radiative corrections to the Higgs sector*, *Phys. Lett.* **B302** (1993) 435–441, [[hep-ph/9207267](#)].
- [61] A. Pomarol and R. Vega, *Constraints on CP violation in the Higgs sector from the rho parameter*, *Nucl. Phys.* **B413** (1994) 3–15, [[hep-ph/9305272](#)].
- [62] J. M. Gerard and M. Herquet, *A Twisted custodial symmetry in the two-Higgs-doublet model*, *Phys. Rev. Lett.* **98** (2007) 251802, [[hep-ph/0703051](#)].
- [63] B. Grzadkowski, M. Maniatis, and J. Wudka, *The bilinear formalism and the custodial symmetry in the two-Higgs-doublet model*, *JHEP* **11** (2011) 030, [[arXiv:1011.5228](#)].
- [64] H. E. Haber and D. O’Neil, *Basis-independent methods for the two-Higgs-doublet model III: The CP-conserving limit, custodial symmetry, and the oblique parameters S, T, U*, *Phys. Rev.* **D83** (2011) 055017, [[arXiv:1011.6188](#)].
- [65] **ATLAS** Collaboration, M. Aaboud et al., *Search for heavy resonances decaying into WW in the $e\nu\mu\nu$ final state in pp collisions at $\sqrt{s} = 13$ TeV with the ATLAS detector*, *Eur. Phys. J.* **C78** (2018), no. 1 24, [[arXiv:1710.01123](#)].
- [66] **ATLAS** Collaboration, M. Aaboud et al., *Search for heavy ZZ resonances in the $\ell^+\ell^-\ell^+\ell^-$ and $\ell^+\ell^-\nu\bar{\nu}$ final states using protonproton collisions at $\sqrt{s} = 13$ TeV with the ATLAS detector*, *Eur. Phys. J.* **C78** (2018), no. 4 293, [[arXiv:1712.06386](#)].
- [67] **CMS** Collaboration, A. M. Sirunyan et al., *Search for beyond the standard model Higgs bosons decaying into a $b\bar{b}$ pair in pp collisions at $\sqrt{s} = 13$ TeV*, [arXiv:1805.12191](#).
- [68] **ATLAS** Collaboration, G. Aad et al., *Constraints on new phenomena via Higgs boson couplings and invisible decays with the ATLAS detector*, *JHEP* **11** (2015) 206, [[arXiv:1509.00672](#)].
- [69] **CMS** Collaboration, V. Khachatryan et al., *Searches for invisible decays of the Higgs boson in pp collisions at $\sqrt{s} = 7, 8$, and 13 TeV*, *JHEP* **02** (2017) 135, [[arXiv:1610.09218](#)].
- [70] N. F. Bell, G. Busoni, and I. W. Sanderson, *Self-consistent Dark Matter Simplified Models with an s-channel scalar mediator*, *JCAP* **1703** (2017), no. 03 015, [[arXiv:1612.03475](#)].
- [71] N. F. Bell, G. Busoni, and I. W. Sanderson, *Two Higgs Doublet Dark Matter Portal*, *JCAP* **1801** (2018), no. 01 015, [[arXiv:1710.10764](#)].

- [72] R. Mahbubani and L. Senatore, *The Minimal model for dark matter and unification*, *Phys. Rev.* **D73** (2006) 043510, [[hep-ph/0510064](#)].
- [73] R. Enberg, P. J. Fox, L. J. Hall, A. Y. Papaioannou, and M. Papucci, *LHC and dark matter signals of improved naturalness*, *JHEP* **11** (2007) 014, [[arXiv:0706.0918](#)].
- [74] T. Cohen, J. Kearney, A. Pierce, and D. Tucker-Smith, *Singlet-Doublet Dark Matter*, *Phys. Rev.* **D85** (2012) 075003, [[arXiv:1109.2604](#)].
- [75] C. Cheung and D. Sanford, *Simplified Models of Mixed Dark Matter*, *JCAP* **1402** (2014) 011, [[arXiv:1311.5896](#)].
- [76] A. Berlin, S. Gori, T. Lin, and L.-T. Wang, *Pseudoscalar Portal Dark Matter*, *Phys. Rev.* **D92** (2015) 015005, [[arXiv:1502.06000](#)].
- [77] G. Arcadi, *2HDM portal for Singlet-Doublet Dark Matter*, [[arXiv:1804.04930](#)].
- [78] M. Bauer, M. Klassen, and V. Tenorth, *Universal Properties of Pseudoscalar Mediators*, [[arXiv:1712.06597](#)].
- [79] N. G. Deshpande and E. Ma, *Pattern of Symmetry Breaking with Two Higgs Doublets*, *Phys. Rev.* **D18** (1978) 2574.
- [80] R. Barbieri, L. J. Hall, and V. S. Rychkov, *Improved naturalness with a heavy Higgs: An Alternative road to LHC physics*, *Phys. Rev.* **D74** (2006) 015007, [[hep-ph/0603188](#)].
- [81] Q.-H. Cao, E. Ma, and G. Rajasekaran, *Observing the Dark Scalar Doublet and its Impact on the Standard-Model Higgs Boson at Colliders*, *Phys. Rev.* **D76** (2007) 095011, [[arXiv:0708.2939](#)].
- [82] E. Dolle, X. Miao, S. Su, and B. Thomas, *Dilepton Signals in the Inert Doublet Model*, *Phys. Rev.* **D81** (2010) 035003, [[arXiv:0909.3094](#)].
- [83] X. Miao, S. Su, and B. Thomas, *Trilepton Signals in the Inert Doublet Model*, *Phys. Rev.* **D82** (2010) 035009, [[arXiv:1005.0090](#)].
- [84] M. Gustafsson, S. Rydbeck, L. Lopez-Honorez, and E. Lundstrom, *Status of the Inert Doublet Model and the Role of multileptons at the LHC*, *Phys. Rev.* **D86** (2012) 075019, [[arXiv:1206.6316](#)].
- [85] G. Belanger, B. Dumont, A. Goudelis, B. Herrmann, S. Kraml, and D. Sengupta, *Dilepton constraints in the Inert Doublet Model from Run 1 of the LHC*, *Phys. Rev.* **D91** (2015), no. 11 115011, [[arXiv:1503.07367](#)].
- [86] A. Ilnicka, M. Krawczyk, and T. Robens, *Inert Doublet Model in light of LHC Run I and astrophysical data*, *Phys. Rev.* **D93** (2016), no. 5 055026, [[arXiv:1508.01671](#)].
- [87] P. Poulose, S. Sahoo, and K. Sridhar, *Exploring the Inert Doublet Model through the dijet plus missing transverse energy channel at the LHC*, *Phys. Lett.* **B765** (2017) 300–306, [[arXiv:1604.03045](#)].
- [88] A. Datta, N. Ganguly, N. Khan, and S. Rakshit, *Exploring collider signatures of the inert Higgs doublet model*, *Phys. Rev.* **D95** (2017), no. 1 015017, [[arXiv:1610.00648](#)].
- [89] M. Hashemi and S. Najjari, *Observability of Inert Scalars at the LHC*, *Eur. Phys. J.* **C77** (2017), no. 9 592, [[arXiv:1611.07827](#)].
- [90] **LHC Higgs Cross Section Working Group** Collaboration, D. de Florian et al., *Handbook of LHC Higgs Cross Sections: 4. Deciphering the Nature of the Higgs Sector*, [[arXiv:1610.07922](#)].

- [91] A. Belyaev, G. Cacciapaglia, I. P. Ivanov, F. Rojas-Abatte, and M. Thomas, *Anatomy of the Inert Two Higgs Doublet Model in the light of the LHC and non-LHC Dark Matter Searches*, *Phys. Rev.* **D97** (2018), no. 3 035011, [[arXiv:1612.00511](#)].
- [92] B. Dutta, G. Palacio, J. D. Ruiz-Alvarez, and D. Restrepo, *Vector Boson Fusion in the Inert Doublet Model*, *Phys. Rev.* **D97** (2018), no. 5 055045, [[arXiv:1709.09796](#)].
- [93] S. von Buddenbrock, N. Chakrabarty, A. S. Cornell, D. Kar, M. Kumar, T. Mandal, B. Mellado, B. Mukhopadhyaya, R. G. Reed, and X. Ruan, *Phenomenological signatures of additional scalar bosons at the LHC*, *Eur. Phys. J.* **C76** (2016), no. 10 580, [[arXiv:1606.01674](#)].
- [94] **ATLAS Collaboration**, M. Aaboud et al., *Search for dark matter in association with a Higgs boson decaying to two photons at $\sqrt{s} = 13$ TeV with the ATLAS detector*, *Phys. Rev.* **D96** (2017), no. 11 112004, [[arXiv:1706.03948](#)].
- [95] **ATLAS Collaboration**, M. Aaboud et al., *Search for Dark Matter Produced in Association with a Higgs Boson Decaying to $b\bar{b}$ using 36 fb^{-1} of pp collisions at $\sqrt{s} = 13$ TeV with the ATLAS Detector*, *Phys. Rev. Lett.* **119** (2017), no. 18 181804, [[arXiv:1707.01302](#)].
- [96] **CMS Collaboration**, *Search for a heavy resonance decaying into a vector boson and a Higgs boson in semileptonic final states at $\sqrt{s} = 13$ TeV*, Tech. Rep. CMS-PAS-B2G-17-004, CERN, Geneva, 2018.
- [97] G. Polesello, *Turning every stone at the LHC: diverse signatures with the 2HDM+a model*, in *Dark Matter @ LHC 2018, Heidelberg, Germany, April 3-6, 2018*.
- [98] **ATLAS Collaboration**, M. Aaboud et al., *Search for an invisibly decaying Higgs boson or dark matter candidates produced in association with a Z boson in pp collisions at $\sqrt{s} = 13$ TeV with the ATLAS detector*, *Phys. Lett.* **B776** (2018) 318–337, [[arXiv:1708.09624](#)].
- [99] **CMS Collaboration**, A. M. Sirunyan et al., *Search for new physics in events with a leptonically decaying Z boson and a large transverse momentum imbalance in proton-proton collisions at $\sqrt{s} = 13$ TeV*, [[arXiv:1711.00431](#)].
- [100] D. Pinna, A. Zucchetta, M. R. Buckley, and F. Canelli, *Single top quarks and dark matter*, *Phys. Rev.* **D96** (2017), no. 3 035031, [[arXiv:1701.05195](#)].
- [101] T. Plehn, J. Thompson, and S. Westhoff, *Dark Matter from Electroweak Single Top Production*, [[arXiv:1712.08065](#)].
- [102] P. Konar, K. Kong, K. T. Matchev, and M. Park, *Dark Matter Particle Spectroscopy at the LHC: Generalizing $M(T_2)$ to Asymmetric Event Topologies*, *JHEP* **04** (2010) 086, [[arXiv:0911.4126](#)].
- [103] C. G. Lester and B. Nachman, *Bisection-based asymmetric M_{T2} computation: a higher precision calculator than existing symmetric methods*, *JHEP* **03** (2015) 100, [[arXiv:1411.4312](#)].
- [104] C. G. Lester and D. J. Summers, *Measuring masses of semiinvisibly decaying particles pair produced at hadron colliders*, *Phys. Lett.* **B463** (1999) 99–103, [[hep-ph/9906349](#)].
- [105] A. Barr, C. Lester, and P. Stephens, *$m(T_2)$: The Truth behind the glamour*, *J. Phys.* **G29** (2003) 2343–2363, [[hep-ph/0304226](#)].
- [106] **ATLAS Collaboration**, M. Aaboud et al., *Search for dark matter produced in association with bottom or top quarks in $\sqrt{s} = 13$ TeV pp collisions with the ATLAS detector*, *Eur. Phys. J.* **C78** (2018), no. 1 18, [[arXiv:1710.11412](#)].

- [107] **CMS Collaboration** Collaboration, *Search for dark matter produced in association with a top quark pair at $\sqrt{s} = 13$ TeV*, Tech. Rep. CMS-PAS-EXO-16-049, CERN, Geneva, 2018.
- [108] U. Haisch, P. Pani, and G. Polesello, *Determining the CP nature of spin-0 mediators in associated production of dark matter and $t\bar{t}$ pairs*, *JHEP* **02** (2017) 131, [[arXiv:1611.09841](#)].
- [109] **ATLAS Collaboration**, M. Aaboud et al., *Search for dark matter and other new phenomena in events with an energetic jet and large missing transverse momentum using the ATLAS detector*, *JHEP* **01** (2018) 126, [[arXiv:1711.03301](#)].
- [110] **CMS Collaboration**, A. M. Sirunyan et al., *Search for new physics in final states with an energetic jet or a hadronically decaying W or Z boson and transverse momentum imbalance at $\sqrt{s} = 13$ TeV*, *Phys. Rev.* **D97** (2018), no. 9 092005, [[arXiv:1712.02345](#)].
- [111] K. J. F. Gaemers and F. Hoogeveen, *Higgs Production and Decay Into Heavy Flavors With the Gluon Fusion Mechanism*, *Phys. Lett.* **146B** (1984) 347–349.
- [112] D. Dicus, A. Stange, and S. Willenbrock, *Higgs decay to top quarks at hadron colliders*, *Phys. Lett.* **B333** (1994) 126–131, [[hep-ph/9404359](#)].
- [113] W. Bernreuther, M. Flesch, and P. Haberl, *Signatures of Higgs bosons in the top quark decay channel at hadron colliders*, *Phys. Rev.* **D58** (1998) 114031, [[hep-ph/9709284](#)].
- [114] R. Frederix and F. Maltoni, *Top pair invariant mass distribution: A Window on new physics*, *JHEP* **01** (2009) 047, [[arXiv:0712.2355](#)].
- [115] B. Hespel, F. Maltoni, and E. Vryonidou, *Signal background interference effects in heavy scalar production and decay to a top-anti-top pair*, *JHEP* **10** (2016) 016, [[arXiv:1606.04149](#)].
- [116] N. Craig, F. D’Eramo, P. Draper, S. Thomas, and H. Zhang, *The Hunt for the Rest of the Higgs Bosons*, *JHEP* **06** (2015) 137, [[arXiv:1504.04630](#)].
- [117] J. Hajer, Y.-Y. Li, T. Liu, and J. F. H. Shiu, *Heavy Higgs Bosons at 14 TeV and 100 TeV*, *JHEP* **11** (2015) 124, [[arXiv:1504.07617](#)].
- [118] S. Gori, I.-W. Kim, N. R. Shah, and K. M. Zurek, *Closing the Wedge: Search Strategies for Extended Higgs Sectors with Heavy Flavor Final States*, *Phys. Rev.* **D93** (2016), no. 7 075038, [[arXiv:1602.02782](#)].
- [119] M. Carena and Z. Liu, *Challenges and opportunities for heavy scalar searches in the $t\bar{t}$ channel at the LHC*, *JHEP* **11** (2016) 159, [[arXiv:1608.07282](#)].
- [120]
- [121] G. Cowan, *Discovery sensitivity for a counting experiment with background uncertainty*, tech. rep., Royal Holloway, London, (2012). Available [online] <http://www.pp.rhul.ac.uk/~cowan/stat/medsig/medsigNote.pdf>.
- [122] **ATLAS Collaboration**, M. Aaboud et al., *Search for top-squark pair production in final states with one lepton, jets, and missing transverse momentum using 36 fb⁻¹ of $\sqrt{s} = 13$ TeV pp collision data with the ATLAS detector*, *JHEP* **06** (2018) 108, [[arXiv:1711.11520](#)].